Geophys. J. Int. (2008) **173,** 168–188 doi: 10.1111/j.1365-246X.2007.03689.x

Influence of the Iceland mantle plume on oceanic crust generation in the North Atlantic

C. J. Parkin and R. S. White

Bullard Laboratories, Madingley Rise, Madingley Road, Cambridge CB3 0EZ, *UK. E-mail: rsw1@cam.ac.uk*

Accepted 2007 November 16. Received 2007 November 2; in original form 2006 November 23

SUMMARY

When a mantle plume with elevated temperature underlies an oceanic spreading centre it affects the generation of oceanic crust by creating thicker crust. We map the variation in crustal thickness and seismic velocity along three long-offset seismic profiles acquired over oceanic crust generated shortly after continental breakup in the North Atlantic: a 212-km-long flowline from the Faroes rifted continental margin across crust of 51–42 Ma age, where oceanic spreading developed close to the inferred centre of the Iceland mantle plume; a 256 km flowline extending from the Hatton rifted continental margin across crust of 52–40 Ma age, about 800 km south of the presumed centre of the mantle plume; and a 99 km strike line over oceanic crust formed at 43 Ma in the Iceland Basin off the Hatton continental margin. The crustal velocity structure along each profile is constrained by multichannel seismic reflection data, which is used primarily to map the sediments, and by densely spaced ocean-bottom seismometers, which recorded wide-angle reflections and refractions to offsets of more than 100 km. Over 56 000 crustal diving wave and Moho wide-angle reflection arrivals were used in joint crustal refraction and reflection tomographic inversions. Quantitative error analysis shows that the seismic velocity of the crust is mostly constrained to within 0.1 km s^{-1} and the depth of the Moho to within $\pm$250 m. We interpret the crustal thickness and velocity changes along the profiles as caused primarily by changes in the mantle temperature at the time of crustal formation. If all the oceanic crustal thickness variations are ascribed to mantle temperature changes, we infer that as mature seafloor spreading developed following continental breakup, the mantle cooled by *ca*. 75 °C over a 10 Myr period, although it still remained hotter than the global average of normal oceanic crust. The crust formed close to Iceland is at all times thicker than that formed further away, which we interpret as reflecting higher temperatures close to the centre of the thermal anomaly created by the mantle plume. Currently at the Reykjanes Ridge, south of Iceland, we interpret thicker than normal oceanic crust as being caused by the presence of hotter mantle, modulated by thickness variations of 1.5–2.0 km which are attributed to temporal variations in the mantle plume temperature of about 25 °C on a 3–6 Myr timescale. A 1.5 km increase in thickness of oceanic crust generated between 48 and 45 Ma on the Faroes line is similar in magnitude and duration to those occurring on the present day Reykjanes Ridge, which we suggest is due to a temperature pulse of ∼25 °C. Gravity lineations in the northern North Atlantic suggest that the oceanic crust has exhibited small thickness fluctuations of similar size throughout its history, interpreted as due to small fluctuations in the temperature of the Iceland mantle plume.

Key words: Tomography; Controlled source seismology; Mid-ocean ridge processes; Continental margins: divergent; Hotspots; Atlantic Ocean.

1 INTRODUCTION

Oceanic crust provides a temporal record of mantle melting processes because it is formed by the melting of mantle welling up beneath an oceanic rift as spreading proceeds. By mapping the thickness and seismic velocity of the oceanic crust generated along two flowlines shortly after continental breakup in the northern North Atlantic we are able to investigate the history of mantle melting and hence the mantle temperature in this region over a period of 12 Myr during the Eocene. In this paper, we consider only crust generated unambiguously at an oceanic spreading centre with clear seafloor spreading anomalies, thus avoiding complications that may arise from mixed continental and oceanic crust in the region of the continent–ocean transition (COT).

One of the main factors controlling the generation of melt beneath seafloor spreading centres, and hence the thickness of the oceanic

crust is the temperature of the mantle (Klein & Langmuir 1987; McKenzie & Bickle 1988). Mantle melting under oceanic spreading centres is extremely sensitive to the temperature of the mantle: an increase in mantle temperature of 50 °C, a change of less than 5 per cent of the normal mantle potential temperature of ∼1300°C, causes a 50 per cent increase in the volume of melt and hence 50 per cent thicker oceanic crust (Bown & White 1994; White 1997). An example of the effect of small quasi-periodic variations in oceanic crustal thickness occurs on the Reykjanes Ridge, south of Iceland. Here, V-shaped ridges of thickened oceanic crust have been interpreted as caused by variations of up to 30 °C in the temperature of the underlying mantle on a timescale of about 3–6 Myr (Vogt 1971; White *et al.* 1995; Smallwood & White 1998; Ito 2001).

Three other factors also control the amount of melt generated under seafloor spreading centres. The first is the composition of the mantle. The consistency of the majority of Mid-Ocean Ridge Basalt (MORB) compositions and the uniformity of oceanic crustal thickness across a range of spreading rates from 15 to 150 mm a^{-1} (White *et al.* 2001), point to a broad uniformity in mantle composition. This is unsurprising, since the spreading centres circle the entire globe, and so cut across a wide range of well-mixed upper mantle. However, in some areas differences in the fertility of the mantle, caused for example, by the presence of subducted lithosphere or of previously depleted mantle may cause variations in the amount of melt generated from mantle at a given temperature (Sallarès *et al.* 2005). The presence of more fusible mantle has been proposed as an explanation for thick igneous crust in the North Atlantic, particularly for melts formed beneath Iceland (Foulger & Anderson 2005), and during the initial continental breakup phase (Korenaga 2004).

Another factor is the presence of volatiles and particularly of water in the mantle. These lower the solidus temperature markedly (Braun *et al.* 2000). Although there are significant volumes of volatiles in backarc basins, which are introduced into the overlying mantle by subducting slabs, there is probably only a small percentage of volatiles in normal upper mantle. This is rapidly incorporated into the melts, and the remainder of the subsequent melting is under dry conditions. Once the volatiles have been removed from the mantle source, the mantle temperature again dominates the amount of melt produced beneath a spreading centre, although the dehydration and concomitant increase in viscosity of the mantle may affect the mantle flow, particularly where a mantle plume is involved (Ito *et al.* 1999; Braun *et al.* 2000; Ito 2001; Maclennan *et al.* 2001).

The third factor is the presence of active upwelling. If the mantle upwelling under the spreading centre is purely passive (i.e. it is corner flow driven by the plate separation), then the rate of melt production by decompression melting of mantle at a given temperature is proportional to the rate of plate spreading. However, if there is a component of active upwelling, such as might be produced by an underlying mantle plume, then the amount of melt produced also depends on the rate of mantle upwelling: if the active upwelling rate is far higher than the rate driven by passive upwelling beneath separating plates then far more melt may be generated (e.g. Korenaga *et al.* 2002; Sallarès *et al.* 2005). Note that there may also be some local buoyancy-enhanced active flow in otherwise passive mantle upwelling caused by the presence of melt in the matrix in the region of decompression melting under the spreading centre (Braun *et al.* 2000), although this is likely to have only a relatively small effect on crustal thickness at the spreading rates of the areas we are studying (Sallarès *et al.* 2005).

In this paper, we assume that the temperature of the mantle is the main control on the amount of melt generated at the North Atlantic oceanic spreading centres for the first 12 Myr after continental breakup for which we have data. In Section 7 near the end of this paper we consider alternative explanations that have been proposed for the variations in crustal thickness and seismic velocity, including the effects of volatiles, of variations in the composition of the mantle, of alteration and cracking of the oceanic crust and fractionation of melts during crustal genesis.

We show results from two seismic surveys over northern North Atlantic oceanic crust formed shortly after continental breakup. Our data is from the integrated Seismic Imaging and Modelling of Margins (iSIMM) project (White *et al.* 2002). Three profiles (Fig. 1) were surveyed in the summer of 2002 adjacent to the Faroes and Hatton continental margins. This paper reports results from the oceanic sections of those surveys in order to investigate changes in melt production during the seafloor spreading following continental breakup. By using only oceanic crust with clear seafloor spreading magnetic anomalies, we avoid complications caused to both the crustal thickness and the mean crustal velocity measurements created by the presence of residual continental crust in the COT. A further advantage of restricting our analysis to oceanic crust is that if there are along-margin variations in the style of rifting in different segments, these may affect magmatic production in the ocean–continent transition, but would not be expected to affect the melting during subsequent mature seafloor spreading.

The Faroes profile, located ∼100 km north of the Faroe–Iceland Ridge (FIR) traverses 212 km of oceanic crust in the Norwegian Basin, while the Hatton line, 800 km south of the FIR, crosses 256 km of oceanic crust in the Iceland Basin. Both near-offset multichannel seismic (MCS) data and wide-angle ocean-bottom seismometer (OBS) data were acquired to allow well constrained determination of the structure and seismic velocity of sediment layers above the basement and modelling of the deeper crustal refractions and Moho reflections. We show evidence for a pulse in the temperature of the mantle plume from 48 to 45 Ma similar to those that are inferred to have formed the V-shaped ridges seen south of Iceland at the present day Reykjanes Ridge. Together with the presence of lineated gravity anomalies in the oldest oceanic crust adjacent to the continental margins, this suggests that the parameters controlling the amount of melt generated, of which we consider the main one to be the temperature of the Iceland mantle plume, may have been pulsing with a similar amplitude and frequency since at least 50 Ma (Parkin *et al.* 2007).

2 RIFT–PLUME INTERACTIONS IN THE NORTHERN NORTH ATLANTIC

Continental breakup in the northern North Atlantic occurred during the Palaeocene (Saunders *et al.* 1997), creating the Reykjanes and Aegir Ridges (Fig. 1). Prior to the continental breakup, NW–SE oriented extension opened a number of NE–SW trending basins parallel to the Atlantic rift (Dóre *et al.* 1997; Ziegler 1989). These basins include the Møre and Vøring basins off Norway, the Faroe–Shetland Basin, and the Hatton–Rockall Basin.

The Iceland mantle plume probably initiated at 62–61 Ma, some 5 Myr before continental breakup (Saunders *et al.* 1997; Jolley & Bell 2002), resulting in the onset of widespread volcanism. Mantle thermal anomalies deduced from basalts emplaced in the Scottish Hebrides (Kent 1995), in Greenland's Baffin Bay (Gill *et al.* 1995) and offshore the east coast of Greenland (Fitton *et al.* 2000) are reported as 50–110, 240–300 and 100 °C above normal, respectively. A

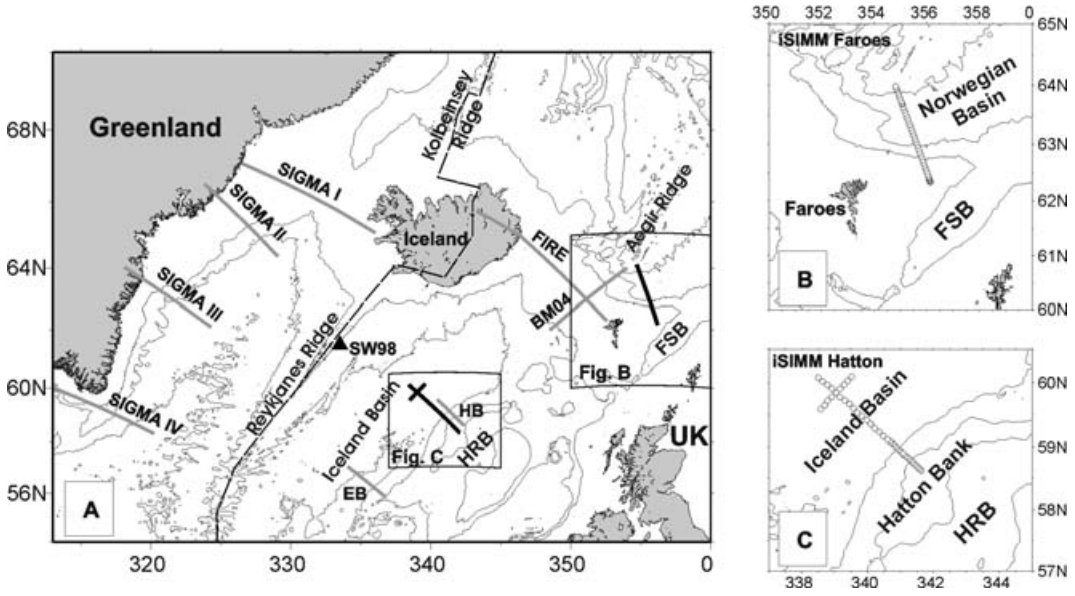

Figure 1. The North Atlantic. Grey lines show existing seismic surveys in the region: SIGMA I-IV off the Greenland margin (Holbrook *et al.* 2001); EB across Edoras Bank (Barton & White 1997); SW98 on the Reykjanes Ridge (Smallwood & White 1998); HB across Hatton Bank (Spence *et al.* 1989; Fowler *et al.* 1989; Morgan *et al.* 1989); FIRE along the Faroe–Iceland Ridge (Smallwood *et al.* 1999); BM04 across the Faroe–Iceland Ridge (Bohnhoff & Makris 2004). HRB is Hatton–Rockall Basin, FSB is Faroe–Shetland Basin. Black lines and Panels (b) and (c) show the iSIMM Faroes and Hatton surveys, respectively. Circles mark OBS positions from which data was used for this study. Bathymetry contour interval 1000 m.

brief hiatus in volcanism followed the earliest phase, until 56–53 Ma when a second, more sustained period of volcanism accompanied the onset of seafloor spreading in the North Atlantic (Saunders *et al.* 1997). During this second phase of widespread volcanism the ubiquitous seaward dipping reflector (SDR) sequences were generated along the continental margins. SDR sequences form when basalts from an elevated rift flow towards the adjacent continent; as rifting continues the region subsides and the SDRs acquire a seaward dip (Mutter *et al.* 1982).

Various conceptual models exist for the shape of the Iceland mantle plume at the time of continental breakup. White & McKenzie (1989) postulated a circular planform 1200 km in radius and centred on Iceland. Jones & White (2003) proposed a larger elliptical shaped anomaly which ascribed thickened Eocene oceanic crust at the Gakkel Ridge and Newfoundland Sea to the same mantle plume thermal anomaly. Smallwood & White (2002) noted that the onset of volcanism was probably within 1 Myr across the entire region and that the thickness of intruded igneous material in the lower crust varied little along the 2000 km extent of the continental margin, suggesting that anomalously hot asthenospheric material arrived almost simultaneously beneath the region that subsequently rifted. They suggested that the original thermal anomaly consisted of a quadrapole-junction of vertical connected sheets of asthenospheric mantle each extending about 1200 km from the centre of the anomaly (see fig. 1 of Roberts *et al.* 2005, for a diagram of the extent of these suggested anomalies). Such a quadrapole-junction pattern, as well as triple-junctions of connected sheets have been modelled by Houseman (1990) as characteristic of the initial stages of rising mantle plumes created by boundary layer instabilities in the mantle. Near the surface they develop into axisymmetric plumes centred on the intersection of the spokes of rising mantle sheets. If a quadrapole-junction of hot connected mantle sheets lay beneath the base of the lithosphere when volcanism started in the North Atlantic, it could explain the observed patterns of volcanism and extension and would also explain the transient uplift without accompanying volcanism seen in the northern North Sea distant from the North Atlantic continental breakup (Nadin & Kusznir 1995; Barton & White 1997).

A different type of thermal anomaly was proposed by Nielsen *et al.* (2002), who suggested that a thin subhorizontal sheet of mantle ∼100–200 °C hotter than normal was emplaced beneath the lithosphere by the plume prior to continental breakup. They suggested that when continental breakup occurred this hot mantle decompressed to form a thick layer of melt which moved buoyantly upward into the crust. Nielsen & Hopper (2004) suggested that small-scale convection could occur within this mantle layer until the layer was exhausted and mantle flow reverted to passive upwelling beneath the rift.

Present-day oceanic crust generated at the Reykjanes Ridge spreading centre, up to 1000 km from the centre of the Iceland plume is thicker than normal non-plume influenced oceanic crust, which has an average thickness of 6–7 km (White *et al.* 1992). The increase in thickness towards Iceland along the Reykjanes Ridge is consistent with increasing temperature of the mantle plume towards its centre with crust formed proximal to the plume centre being thicker than that formed further away (White 1997). As well as the spatial effect of the plume there is also a temporal effect of the plume temperature pulsing (White *et al.* 1995). Prominent V-shaped ridges caused by crustal thickness variations are mapped on crust younger than 37 Ma on the Reykjanes and Kolbeinsey Ridges, suggesting mantle temperature fluctuations of ∼25 °C on a timescale of 3–6 Ma (Vogt 1971; White 1997; Smallwood & White 1998; Ito 2001; Jones *et al.* 2002).

Other evidence for temperature oscillations come from the composition of Northern Component water flowing across the Greenland–Iceland–Faroes Ridge. Compositional variations in the water have been interpreted by Wright & Miller (1996) and Poore *et al.* (2006) as being controlled by fluctuations in the temperature of the Iceland mantle plume causing changes in the elevation of the Greenland–Iceland–Faroes Ridge, which then acts as a 'lockgate'

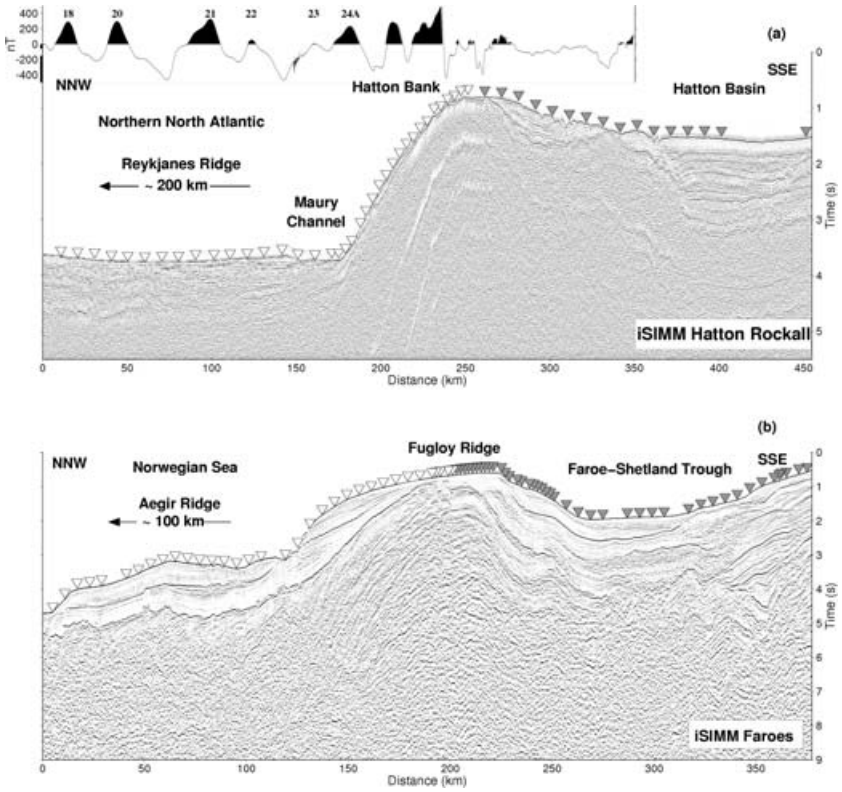

Figure 2. Top panel shows the Hatton iSIMM seismic reflection profile. Bottom panel shows the Faroes iSIMM seismic reflection profile. Note the different scales of these profiles. Inverted triangles show the positions of the OBS deployed along the lines; we only use those marked by open triangles for this study. Magnetic anomaly data with anomaly identification is shown above the Hatton profile.

controlling water flow. Indirect evidence for pulsing of the Iceland mantle plume in the early stages of its history has also been proposed using sedimentation patterns (White & Lovell 1997) and dating of seamounts in the Rockall Trough (O'Connor *et al.* 2000).

In this paper, we interpret variations in the seismic velocity and thickness of the oceanic crust as indicative of variations in the temperature of the mantle from which it was formed, and discuss the constraints this provides on mantle temperature changes immediately following continental breakup.

3 SURVEY DATA

The iSIMM profiles were acquired using the RRS Discovery for OBS wide-angle profiles and the M/V Geco Topaz for the seismic reflection profile along the Faroes line. In this paper, we report results from 34 OBS deployed at a spacing of 6 km over the oceanic crust and adjacent continental margin on the Faroes profile and 46 OBS deployed at a spacing of 4 or 10 km across the oceanic crust and adjacent continental margin on the Hatton profile (Fig. 1). The seismic source for shooting into the OBS arrays was a bubble-tuned 101 l (6340 cubic inches), low-frequency (∼10 Hz), broad-band airgun array designed to optimize deep penetration at large offsets (Lunnon *et al.* 2003). Magnetic and bathymetric data were collected by RRS Discovery. Forty-two Expendable Bathy-Thermographs (XBTs) and a velocimeter were used during the cruise to determine accurately the water column velocity structure. The Faroes margin seismic reflection profile was acquired after the OBS survey using a 12 km streamer deployed from the M/V Geco Topaz, and a 167 l (10 160 cubic inches), low-frequency (∼9–11 Hz dominant frequencies) airgun source (White *et al.* 2002).

3.1 Near-offset MCS

3.1.1 Hatton MCS

The MCS reflection data for the Hatton survey (Fig. 2a) were acquired simultaneously with the shooting into the OBS using a 2.4 km long streamer towed at 18 m depth. Ninety-six streamer groups were recorded with 25 m spacing and a sample rate of 4 ms, to a record length of 15 s. Processing focused on determining the depth to basement and the velocity of the sediments, since penetration into the deeper basement was poor. The shot separation was 150 m to prevent overshooting the OBS profile by creating wrap-around noise: this resulted in a CMP fold of 8 in the MCS profile. CMP supergathers of up to 45-fold were constructed by summing adjacent CMP gathers and were used for an initial velocity analysis, after which a geometrical spreading correction was applied, followed by a second iteration of velocity analysis. Dip moveout correction was used to compensate for dipping layers and then a final velocity analysis was made. A Kirchoff post-stack migration was applied to reduce diffractions and improve identification of the basement reflections.

3.1.2 Faroes MCS

The Faroes MCS profile (Fig. 2b) was acquired by WesternGeco using their Q-Marine™ system, with three streamers deployed for the entire 380-km-long Faroes line. The 12-km long Q-Marine™ streamers recorded single sensors spaced every 3.125 m, which were grouped into 12.5 m sections during processing. A high capacity, 167 l (10 160 cubic inches) bubble tuned source was deployed using

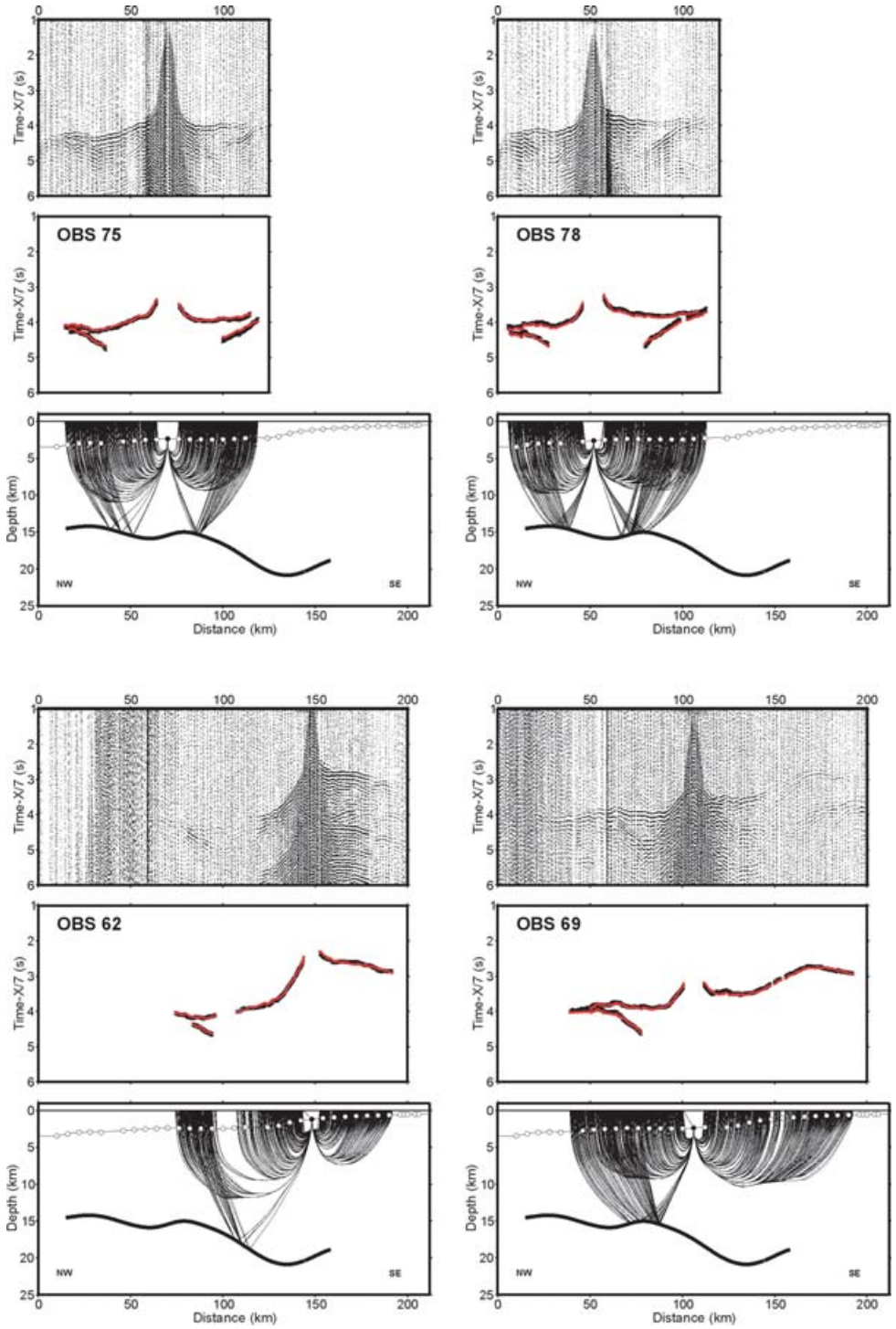

Figure 3. Vertical component geophone data, traveltime picks and model ray coverage from four example OBS on the Faroes profile. For each OBS, the top panel shows the record section reduced at 7 km s^{-1}; middle panel shows the phase arrival picks (black) and those predicted by the model (red); bottom panel shows the ray coverage of each instrument.

48 guns towed at 18 m depth. Each shot was recorded by calibrated near-field hydrophones mounted within 1 m of each gun. Using the notional source algorithm of Ziolkowski *et al.* (1982), the far-field signature was calculated for processing the complex waveform produced by the bubble tuned array. Spitzer *et al.* (2005) provide a detailed description of key features of the Faroes iSIMM reflection data and a comparison to previous reflection surveys in the region.

3.2 Wide-Angle OBS

All seismometers deployed were 4-channel OBS from Geopro comprising a hydrophone and a gimballed type SM-6, 4.5 Hz, three-component geophone. Data were recorded digitally using a 24-bit analogue-digital converter with a dynamic range of 120 dB and a 4 ms sample rate. Figs 3–5 show typical record sections from the vertical geophones of OBS deployed along the profiles, together

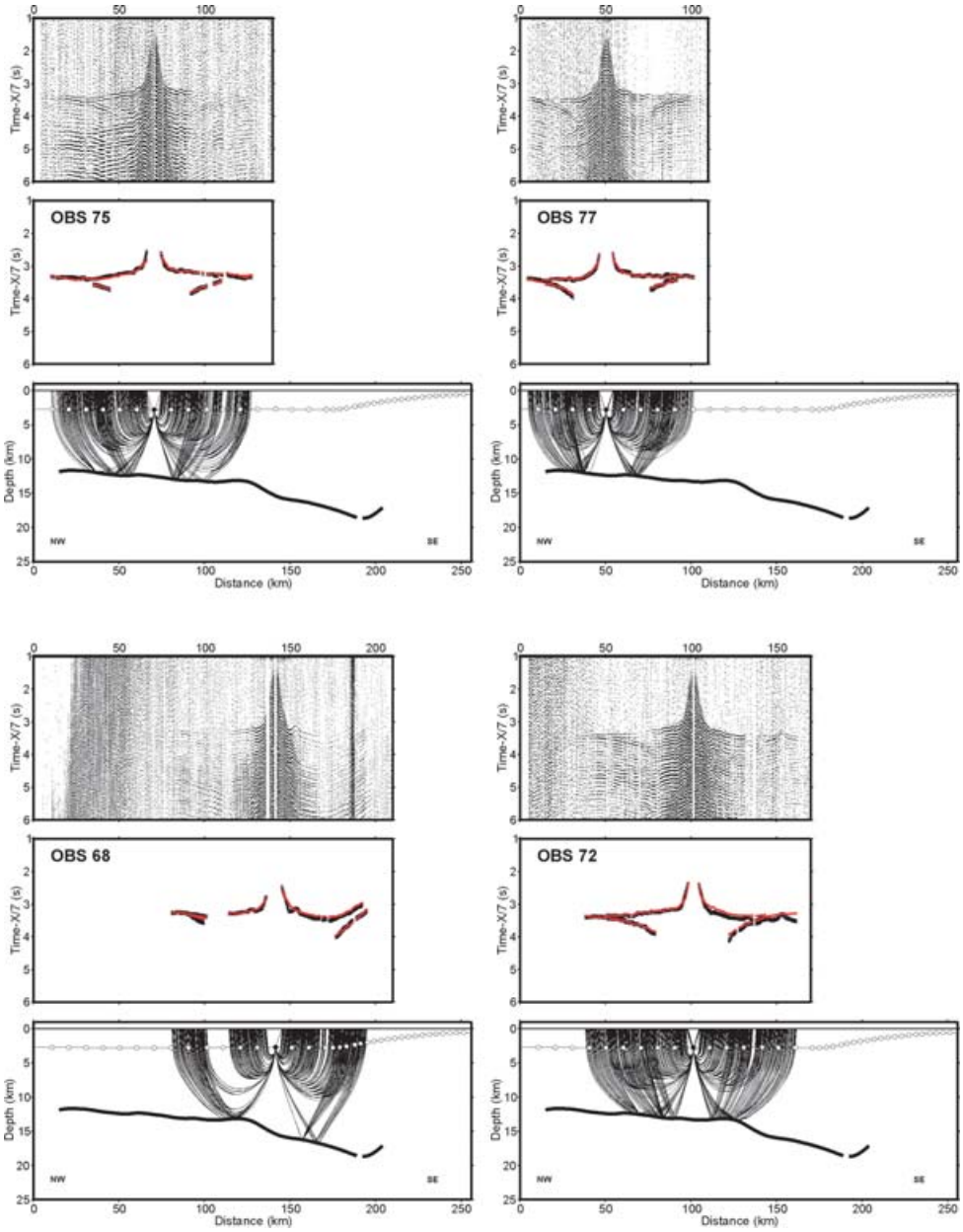

Figure 4. Vertical component geophone data, traveltime picks and model ray coverage from four example OBS on the Hatton dip profile. For each OBS, top panel shows the record section reduced at 7 km s^{-1}; middle panel shows the phase arrival picks (black) and those predicted by the model (red); bottom panel shows the ray coverage of each instrument.

with traveltime fits to the main arrivals and the associated ray paths through the model. Additional vertical hydrophone arrays were deployed for each survey and were used by Lunnon *et al.* (2003) to compare the peak and bubble airgun tuning methods used during acquisition. To reduce the impact of reverberation of seismic energy in the water column, which can obscure the succeeding record with 'wrap-around' noise (Nakamura *et al.* 1987; McBride *et al.* 1994), we required the time interval between shots to be 50 s or more. On the Faroes profile, where we were not towing a streamer, we were able to steam at 4.5–5.5 km h^{-1} to achieve a shot interval of 75 m, while still retaining an interval of more than 50 s between shots. However, on the Hatton profile we acquired simultaneously a seismic reflection profile, so in order to maintain the streamer depth we had to use a higher towing speed of 9.3 km h^{-1}, which necessitated an interval between successive shots of 150 m.

The overall quality of the data is good for all three geophone components. OBS locations were repositioned from their drop positions using the water wave arrivals with an accurate water-layer velocity profile model from the XBT and velocimeter profiles taken during the cruise. The OBS drifted by typically *ca*. 400 m from their surface deployment positions before they reached the seafloor.

4 AGE OF OCEANIC CRUST

To determine the age of the oceanic crust along our profiles, magnetic anomalies were identified from magnetometer data. The ages of the identified anomalies were determined using the timescale of Cande & Kent (1992). For the Hatton line we used data from a towed magnetometer (Fig. 2a), as well as the gridded North Atlantic data of Verhoef *et al.* (1996). The Hatton profile extends from the

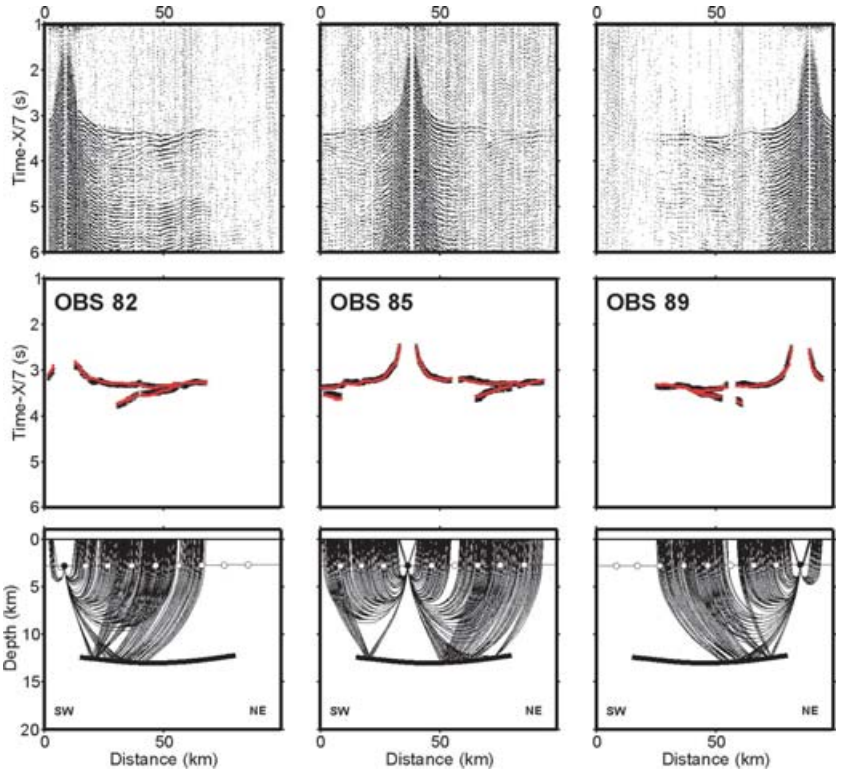

Figure 5. Vertical component geophone data, traveltime picks and model ray coverage from four example OBS on the Hatton strike profile. For each OBS, top panel shows the record section reduced at 7 km s^{-1}; middle panel shows the phase arrival picks (black) and those predicted by the model (red); bottom panel shows the ray coverage of each instrument.

continental margin to 39 Ma crust (chron 18). No magnetic data were collected during acquisition of the Faroes line. Instead we used magnetic anomaly data from ship tracks near the profile and the gridded data of Verhoef *et al.* (1996). In addition, we use the adjacent DSDP drill sites 336 and 337 which both reported basaltic basement ages (Kharin *et al.* 1976). The basaltic basement radiometric age of site 337 is in error and we consider the oldest sediment age above the basement to be a better indication of the basement age here. The Faroes line extends from the continental margin to 42 Ma oceanic crust. Our interpretation of the seafloor spreading at the Aegir Ridge is similar to that from a recent study by Scott *et al.* (2005), with spreading at the Aegir Ridge continuing until chron C17, some 100 km beyond the NNW end of our line.

5 TOMOGRAPHIC MODELLING

We use wide-angle seismic data (diving waves and Moho reflections) from all 34 OBS deployed over oceanic crust of the Norwegian Sea and the adjacent continental margin on the Faroes line and 46 OBS deployed along the two profiles shot over oceanic crust of the Iceland Basin and the adjacent continental margin in the Hatton area (open triangles on Figs 2a and b). Three separate OBS profiles were modelled: two profiles are >200 km long and lie approximately along flowlines, with a shorter 99 km long strike line in the Iceland Basin across oceanic crust formed at 43 Ma (chron C20) (Fig. 1). These profiles are hereafter named the Faroes, Hatton dip and Hatton strike lines. Table 1 shows the number of traveltime picks made along each profile.

For the modelling, the OBS (with locations typically 400 m offline), were repositioned onto the profile and the traveltime picks were corrected to the seafloor. By checking for traveltime reciprocity between shots made close to OBS positions projected onto the profile using Zelt & Smith's (1992) method, we confirmed the consistency of these corrections. Following the wide-angle modelling guidelines of Zelt (1999), traveltime picking errors were assigned to each arrival corresponding to the duration of the first half-cycle of the picked phase. We assigned picking errors of 60 ms for the first arrival Pg phases and 70 ms for the secondary arrival Moho (*PmP*) reflections.

Table 1. Line lengths and traveltime picks.

Line	Length (km)	Pg	*PmP*	Total OBS
Faroes	212	26 282	7447	34
Hatton dip	256	15 353	3441	37
Hatton strike	99	2906	1260	9

Tomographic inversions were used to find best-fitting velocity models from the traveltime data. To produce starting models for the inversions we used a sediment velocity model derived from semblance analysis of the MCS data. We then determined the velocity variation with depth of the best-fitting 1-D crust below these sediments. The combined sediment and 1-D crustal models (Fig. 6) were used as starting models for the tomographic inversions using the tomography code of Korenaga *et al.* (2000) which uses both diving wave and reflection constraints. The Moho was the deepest reflector considered in the inversion.

5.1 Parametrization

For the tomographic inversions we use a grid spacing of 0.5 km horizontally with the vertical nodes hung below the seafloor, increasing

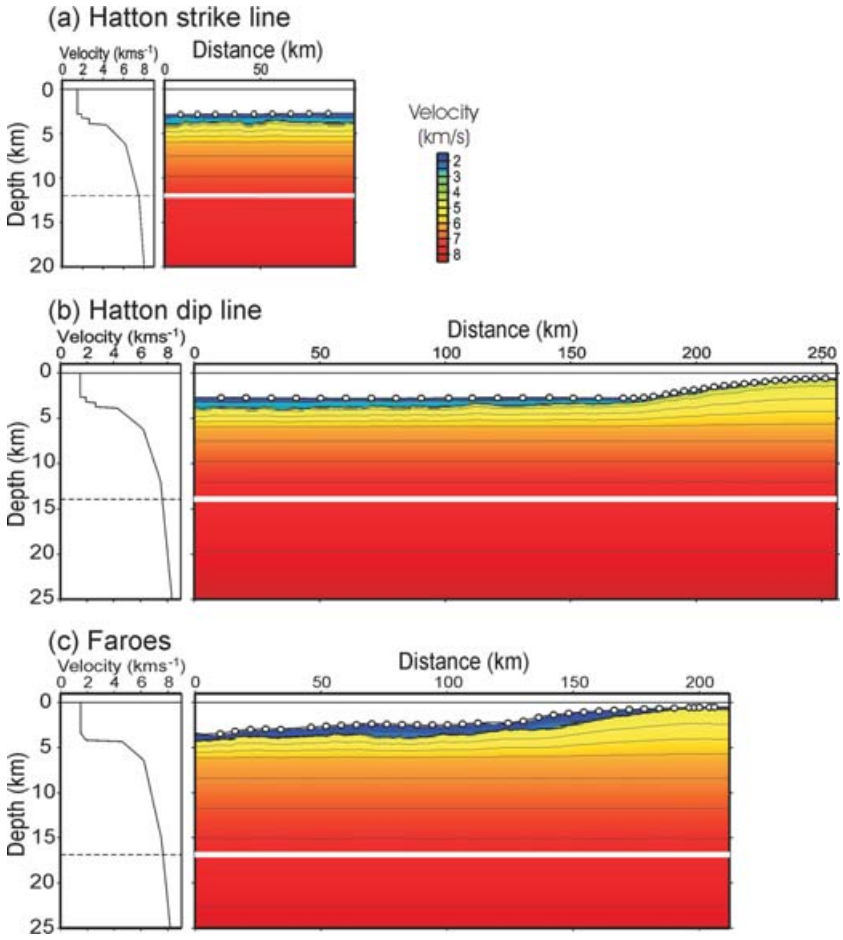

Figure 6. Starting models for the joint refraction and reflection tomographic inversion using the method of Korenaga *et al.* (2000). Starting models were prepared using the MCS data (Fig. 2) for sediment velocities above a best-fitting 1-D crust determined from ray tracing the traveltimes of arrivals from a subset of the OBS. Velocity profiles show the velocity from the left-hand side of each model. Moho is at the depth of the dotted line on the velocity profile and the white line on the models. Circles show OBS positions.

from 50 m spacing at the top of the models to 800 m at the bottom of the models at 30 km depth. We define our correlation lengths to be the approximate resolving power of our data set. The horizontal resolution is controlled by the OBS spacing along each line, giving 4 km near the seafloor, increasing with depth to 6 and 10 km for the Faroes and two Hatton surveys, respectively. The vertical correlation length is based on the size of the first Fresnel zone of the signal recorded by the OBS, and was set as 200 m at the seafloor, increasing to 2.5 km at the base of the models.

In order to stabilize the inversion, smoothing and damping constraints can be applied independently to the model updates in vertical and horizontal directions. This provides four independent ways of constraining the inversion. Following Korenaga *et al.* (2000), we first determine appropriate smoothing constraints to apply to the correlation lengths by examining smoothing versus rms trade-off ('L') curves and by inspection after testing a variety of values across each model. We then fix these smoothing constraints and apply variable damping to the model updates. To restrict the model updates and prevent large swings in the models during the first few iterations we set the damping values (as defined by Korenaga *et al.* 2000) to be 5 per cent for velocity and 10 per cent for depth. These restrain the second-order derivatives in the inversion. The damping was removed for later iterations to ensure that the final model was not closely dependent on the starting model. Prior to inversion the rms misfits of the starting models were 203 ms ($\chi^2 \sim 10$) for the Faroes line, 286 ms ($\chi^2 \sim 20$) for the Hatton dip line and 150 ms ($\chi^2 \sim 7$) for the Hatton strike line. After fewer than ten iterations the final rms misfits are 67 ms ($\chi^2 \sim 1.0$), 66 ms ($\chi^2 \sim 1.1$) and 41 ms ($\chi^2 \sim 0.5$) for the same three lines. Fig. 7 show the reduction of the traveltime residuals before and after inversion while Fig. 8 shows the derivative weight sum (DWS) ray coverage of each line.

6 MODEL UNCERTAINTY ANALYSIS

The uncertainty in tomographic inversions is often assessed using synthetic tests such as checkerboard or spike sensitivity tests (Spakman & Nolet 1988). Synthetic tests determine how well a particular, user defined, synthetic pattern can be recovered by the data, given the particular configuration of sources, receivers, velocity structure and ray paths through it. Where an inversion is regularized by smoothing constraints, as in the code of Korenaga *et al.* (2000), the full detail of the anomalies can never be recovered because the smoothing that is applied to stabilize the inversions allows recovery of only the smoothed crustal structure. The way we have chosen to measure the uncertainty of seismic velocity constraints in our modelling, which uses a non-linear inversion technique, is a Monte Carlo method with multiple random samples of the solution space. The randomization is based on likely information about the

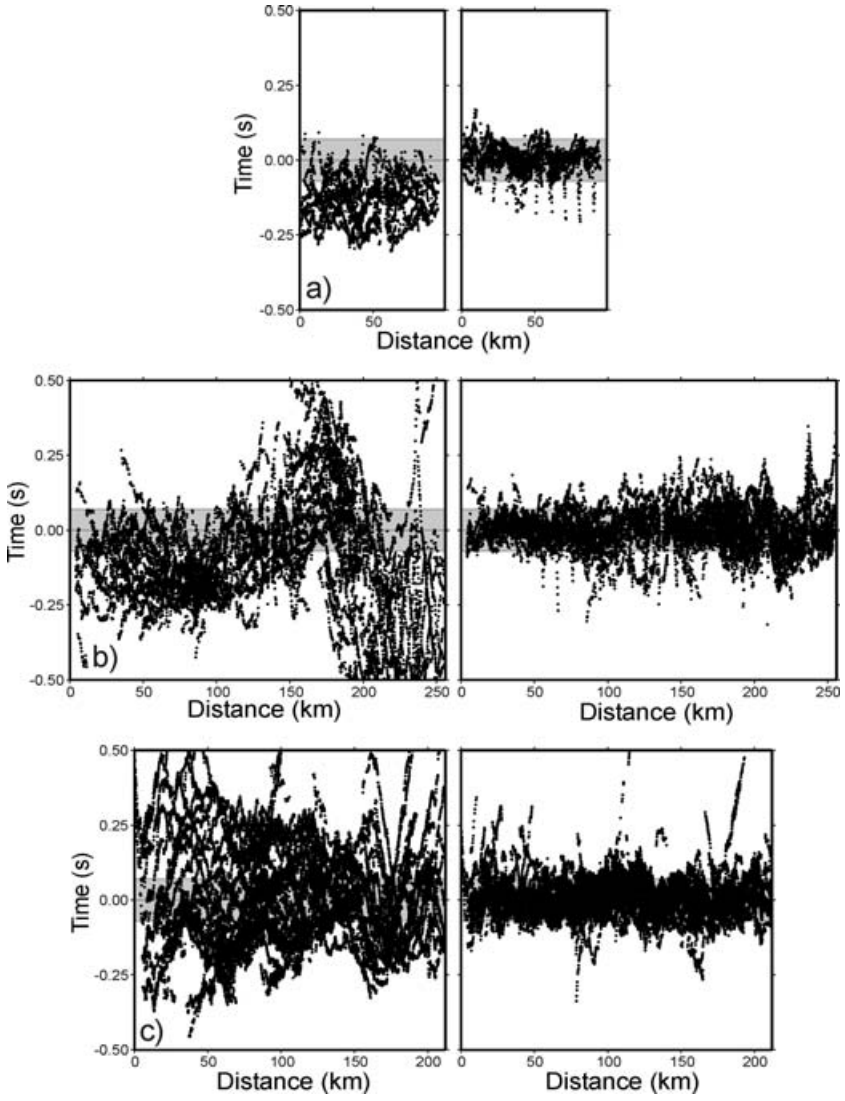

Figure 7. Traveltime residuals across each line before (left-hand panels) and after (right-hand panels) tomographic inversion. From top (a) the Hatton strike line, (b) the Hatton dip line and (c) the Faroes line. Grey bar shows typical errors assigned to traveltime picks.

model so that it searches a particular area of the model space, yet still retains a random element (Gubbins 2004). The *a posteriori* marginal density function $\sigma_M(\mathbf{m})$ is the solution of the inverse problem, combining all information and physical relationships across the model space **m** and can be found from

$$\sigma_M(\mathbf{m}) = \int \sigma(\mathbf{d}, \mathbf{m})\, \mathrm{d}\mathbf{d}, \tag{1}$$

where **d** and **m** are the observable (data) and model parameters, and the probability density $\sigma(\mathbf{d}, \mathbf{m})$ is the *a posteriori* state of information (Tarantola 2005). By taking N samples randomly about **d** and **m** we sample $\mathbf{m}_1, \mathbf{m}_2, \ldots, \mathbf{m}_N$ of $\sigma_M(\mathbf{m})$. Assuming that all N realizations of $\sigma_M(\mathbf{m})$ have the same probability $\frac{1}{N}$, the mean and other statistical measures such as standard deviation σ can be estimated from the velocity models (Mosegaard & Sambridge 2002). By taking the initial randomization about assumed information in **d** and **m** (information such as picking error and knowledge of the velocity model), the random errors map into the *a posteriori* function and statistical methods give a measure of the random values that depend on the data, the model and the physical relationship between them. Both our starting models and traveltime picks were randomized 100 times within the wide bounds shown in Fig. 9.

Using an average 1-D velocity profile with depth the wide range of starting models shown in Fig. 9 were found by randomizing points on the 1-D profile in both velocity and depth. Sediment layer information is known *a priori* from the MCS data. However, because the velocity profile is continuous, the velocity at the base of the sediments was varied by ± 0.3 km s^{-1} and its depth by ± 0.4 km to fully randomize the basaltic oceanic layer 2 below it. Further randomizations in velocity of ± 0.4 and ± 0.5 km s^{-1} were made at the base of oceanic layers 2 and 3, respectively, and an additional randomization of ± 0.25 km s^{-1} was introduced at the base of the model to provide wide sampling of the velocity space. The depths of oceanic layers 2 and 3 were varied by ± 0.25 and ± 3.0 km, respectively. By using a wide range of starting velocities and depths we ensure that the 1-D crustal thickness variations cover the likely bounds of the oceanic crustal structure.

Instead of adding random noise to each individual traveltime pick we follow Zhang & Toksöz (1998), who noted that it is unlikely one would pick truly randomly varying traveltimes on adjacent shots along a phase arrival, because in most cases one identifies the

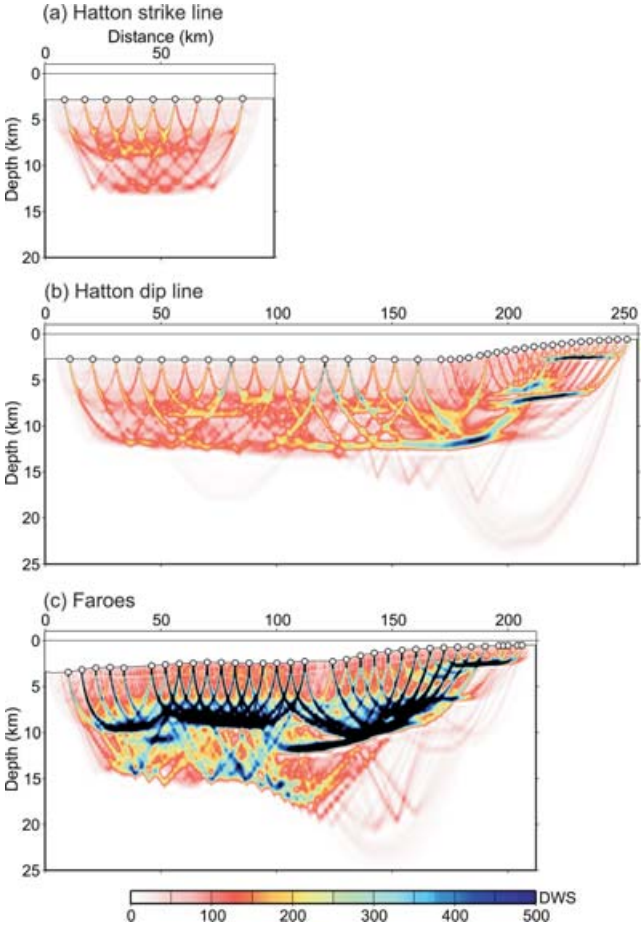

Figure 8. Derivative weight sum (DWS) for all lines. DWS is highest at the Moho (constrained by *PmP* reflections) and within oceanic layer 2 and the top of oceanic layer 3 (constrained by diving waves). The Faroes line has the highest DWS as a result of the more closely spaced instruments and smaller shooting interval.

moveout of a phase across a record section (e.g. Figs 3–5), rather than picking a time based on a single trace. It is more likely that the traveltime picks inadvertently slip from one phase to another, especially in the presence of noise or other interfering arrivals. We therefore randomize traveltimes in a manner similar to that used by Zhang & Toksöz (1998), using a common receiver error as well as a random moveout error across each phase. We assigned three control points for the variations: the start point is at the minimum observed offset of a particular phase; the second point is at the mid-position in the offset ordered picks; and the third point is at the position of maximum offset of that phase. The middle point was randomized to incorporate a *pseudo-random* position where the traveltime gradient changes to simulate a skipping of phase across the picks, which can often happen when picking the arrival times of noisy data. We used a traveltime moveout error of ± 50 ms at the start, decreasing to 0 ms in the middle and then increasing again to ± 50 ms at the end. The common receiver error was set to be one half of the Pg picking error. Combining the two errors, the maximum possible error across the traveltime picks was ± 75, ± 25 and ± 75 ms (i.e. 1.5, 0.5 and 1.5 times the Pg error of 50 ms), at the start, middle and end of each phase arrival, respectively. By varying the traveltime errors in this way we randomize them all by an average of 50 ms while still incorporating the bigger errors of the *PmP* phase at larger offsets.

Each random starting velocity model was inverted with a randomized traveltime data set to obtain 100 Monte Carlo realizations. The average velocity distribution of all 100 tomographic models is shown in Fig. 10, and the standard deviation of the 100 realizations in Fig. 11. The standard deviation of the velocity at any point in the model is typically less than 0.1 km s^{-1}. There is a band of velocities with higher standard deviation of up to 0.2 km s^{-1} present on each profile (Fig. 11), at a depth which corresponds to the sharp transition from relatively low-velocity sediment to the top of basaltic oceanic layer 2, which has typically twice the velocity of the sediment. It may appear paradoxical that there is a large uncertainty in the seismic velocity near such a well-defined interface as that between sediments and the top of the igneous oceanic crust. The reason is that the model is parametrized by discrete depth control nodes, and just a small variation in the steep velocity gradient between nodes from velocities typical of sediments to those typical of basalts causes a large variation in velocity at any particular depth in this interval between model nodes. So the standard deviation of acceptable models in this depth interval increases markedly, even though the overall change in traveltimes may be very small.

There are large areas of the lower crust above the Moho where the standard deviation rises to 0.2 km s^{-1}, which correspond to the areas of low ray coverage (see DWS in Fig. 8) towards the continental end of the profile (right-hand side). Where the ray coverage is good the standard deviation for the depth of the Moho is within 250 m.

In addition to the Monte Carlo test we also test for velocity versus depth trade-off in the lower crust above the Moho, which can be problematic for traveltime tomography where, as is the case for our study, only *PmP* reflections are used to determine the depth to the Moho reflector. Depending on the geometry of the source–receiver pairs and the coverage of the reflections it may be possible to reduce the trade-off between the velocity and depth. Bickel (1990) showed that by increasing the number of multiple offset traveltime picks, the velocity versus depth non-uniqueness might be overcome, providing the offset of the picks span at least three times the lateral variations in velocity. The tomography code of Korenaga *et al.* (2000) provides a method for testing the velocity versus depth problem using the weighting parameter w to adjust the relative weighting of depth sensitivity in the Fréchet matrix. By using $w \neq 1.0$ the model iterations can be forced to preferentially update either the lower crustal velocity or the Moho depth. Any areas of the model subject to large velocity versus depth ambiguity will be revealed by systematically varying w. For our final models we keep $w = 1.0$ which gives equal weighting to both depth and velocity. To test our velocity versus depth trade-off we use $w = 100$ to preferentially update depth changes and $w = 0.01$ to preferentially update velocity changes.

The results of these trade-off tests as well as the reference model with $w = 1.0$ are shown in Fig. 12. For the two long dip lines the difference is only notable at the continental ends where the ray coverage is reduced. By using $w < 1.0$ the Moho is shallower at the continental end and closer to its starting position, since the model has preferentially updated the velocity rather than the depth. The difference between the Moho positions for the Hatton strike line (Fig. 12) is small across all values of w, although the velocity above the Moho was changed further from the starting model when using $w < 1.0$. However, it is the Hatton strike-line that has the smallest offset range across the Moho reflector due to its shorter length, and it should, therefore, exhibit the most velocity versus depth ambiguity. In general, given the receiver geometry, the ray coverage and the large correlation lengths used, the inversions do not suffer from any serious velocity versus depth ambiguity and the rms traveltime residuals of all the models are similar.

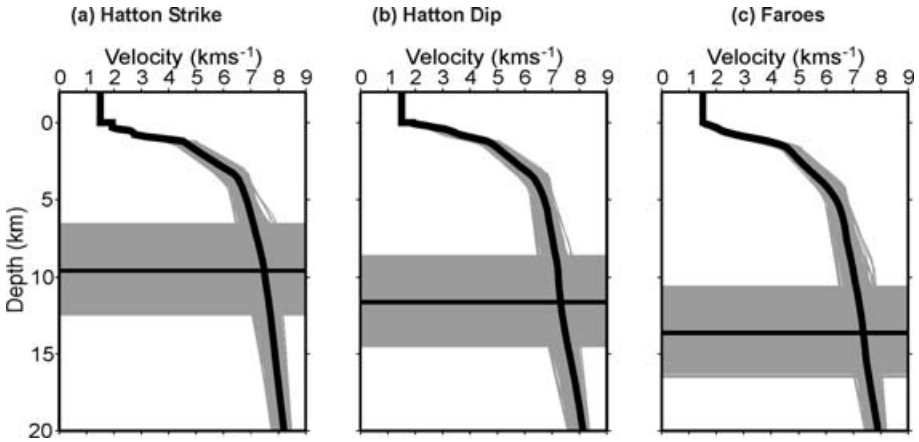

Figure 9. Random starting models for the Monte Carlo analysis. 100 random starting models and Moho positions were taken for each line (grey) about the average profile from an initial inversion of the traveltime data (black). Moho depth (horizontal lines) was varied independently of velocity by ±3 km of the average depth.

7 DISCUSSION

7.1 Velocity structure

Representative velocity–depth profiles of the oceanic igneous crust (i.e. the section beneath sediments), from along the Hatton and Faroes dip lines are shown in Fig. 13. They show the characteristic increase in velocity with depth through the upper 2–3 km of crust (i.e. layer 2 of oceanic crust), from around 4 km s^{-1} at the top of layer 2 to 6.7 km s^{-1} at its base. This increase is a result mainly of the increase in pressure with a concomitant decrease in fractures and pore space, and a decrease in alteration within the extrusive lavas and dykes of the upper oceanic crust. There is a marked inflexion point in the velocity versus depth curve at a velocity of 6.7 km s^{-1}, beneath which the velocity gradient decreases by an order of magnitude from ∼1.0 s^{-1} in layer 2 to ∼0.1 s^{-1} in the underlying lower-crust (oceanic layer 3). We use the velocity of 6.7 km s^{-1} at this inflexion point to define the top of Layer 3, the oceanic lower-crust.

The mean velocity of the lower oceanic crust is everywhere somewhat higher than the global average of 6.95 km s^{-1} for normal oceanic crust determined from a compilation by White *et al.* (1992), reaching nearly 7.3 km s^{-1} where the oceanic crust is thickest. Melting of mantle which is hotter than normal increases the amount of Mg in the melt, which causes higher than normal seismic velocities when the melt freezes in the crust (e.g. White & McKenzie 1989; Kelemen & Holbrook 1995; Korenaga *et al.* 2002; Sallarès *et al.* 2005). Anomalously high lower-crustal velocities in excess of 7.1 km s^{-1}, similar to those reported here, have also been observed in oceanic crust adjacent to other continental margins in the North Atlantic, including the eastern side of Greenland (e.g. Korenaga *et al.* 2000; Holbrook *et al.* 2001; Hopper *et al.* 2003; Voss & Jokat 2007), the northwest European margin (e.g. Fowler *et al.* 1989; Barton & White 1997; Breivik *et al.* 2006), and the Norwegian margin (e.g. Zehnder *et al.* 1990; Mjelde *et al.* 1997, 1998). We discuss later the inferences about mantle temperature and composition that can be drawn from these observations of lower-crustal velocities.

At the continent-ward end of the Hatton and the Faroes dip lines (i.e. at distances greater than 210 and 150 km, respectively), the profiles intersect the crust of the COT. Although heavily intruded by igneous material and with thick extrusive basalts forming SDRs (Fig. 14b), the influence of residual continental crust on the seismic velocity structure in this region can be seen by the abrupt deepening of the 6.5 km s^{-1} velocity contour at the COT (Figs 10b and c). The thick layer with velocities of 5.0–6.5 km s^{-1} is caused by residual continental crust which lies beneath the extrusive lavas and above the main zone of lower-crustal intrusion on the COT. We do not include results from the sections of the profiles that traverse the COT in our interpretation of the oceanic crustal structure discussed later.

7.2 Seaward dipping reflectors

The extrusive basalts on the continental margin show the characteristic arcuate SDR sequences typical of volcanic rifted margins elsewhere in the northern North Atlantic. The smooth arcuate SDRs imaged on the COT of the Faroes profile (Fig. 14b) and those reported by White *et al.* (1987) on the Hatton COT indicate that rifting was initially subaerial and remained so until about C24 time (52 Ma). Similar subaerial SDRs are reported by Larsen & Jakobsdóttir (1988), Larsen & Saunders (1998) and Hopper *et al.* (2003) on the Greenland margin COT conjugate to the Hatton profile prior to C24. Between C24 (52 Ma) and C23 (51 Ma) there is a rough broken hummocky basement below which little is imaged: this is interpreted as marking the change from subaerial to submarine eruptions (Planke *et al.* 2000).

Younger than 51 Ma the rough basement ends and more SDR sequences are seen, but with a lower curvature and dip, and a more broken, irregular nature (Fig. 14a); these are interpreted as submarine SDRs (Planke *et al.* 2000; Parkin *et al.* 2007). In shallow water environments the volcanic extrusions are normally explosive due to magma degassing, resulting in flows that are chaotic in nature. In deep water the gas cannot escape so easily from the extrusive lavas and in these conditions large sheet flows can form if the melt supply is sufficient to flow over local bathymetry (Gregg & Fornari 1998). So we interpret the change from arcuate SDRs through a segment of rough hummocky basement to linear, irregular SDRs as caused by a change from subaerial rifting at the time of continental breakup to submarine seafloor spreading after 51 Ma (anomaly C23 time).

7.3 Oceanic crustal thickness

In order to ensure that we use only crust generated at a mature seafloor spreading centre, we do not in our analysis use crust which

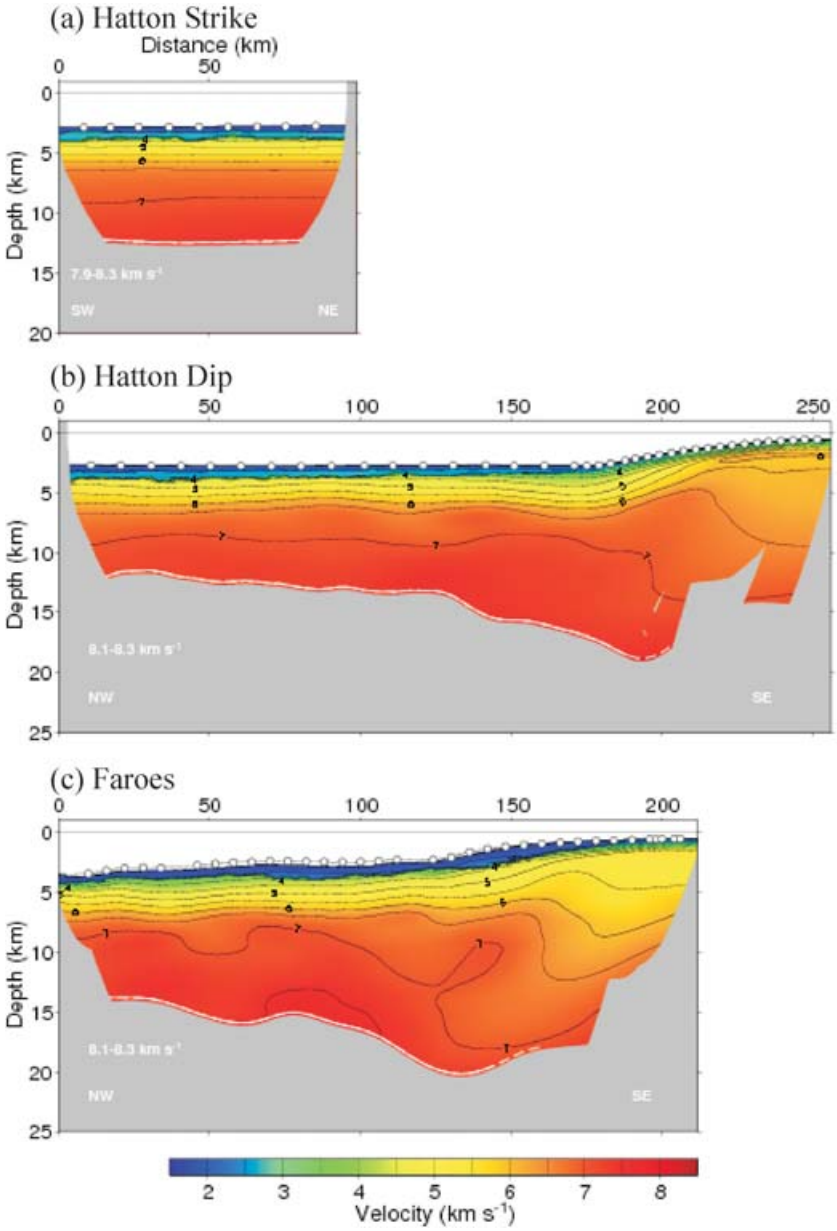

Figure 10. Ensemble average of each line following Monte Carlo analysis. White lines show position of the Moho, dashed lines are where Moho ray coverage is low and the Moho position unreliable. Only those areas where there is ray coverage are coloured. Mantle velocity is determined independently by modelling the *PmP* amplitude variation with angle of incidence. Contours shown at 0.5 km s^{-1} intervals and labelled at 4, 5, 6 and 7 km s^{-1}.

exhibits arcuate SDRs such as those shown in Fig. 14(b). This ensures that we do not include in our analysis any crust from the COT, which may include a proportion of relict continental material, although it also means that the oldest oceanic crust we consider is about 53 Ma old and is, therefore, somewhat younger than the breakup time of about 55 Ma. Nevertheless, we see a clear decrease in oceanic thickness for the first 5–6 Myr of seafloor spreading in the early North Atlantic ocean (Fig. 15). As we show later, the thickness of oceanic crust of the same age on the SIGMA III line off Greenland (Hopper *et al.* 2003), which is approximately conjugate to the Hatton dip profile, is the same within the measurement uncertainty as that of the Hatton profile, as of course we would expect since it was generated at the same time and at the same spreading centre.

The oceanic crust of the Faroes profile is at all times thicker than crust of the same age on the Hatton profile. If the crustal thickness is dependent only on the temperature of the mantle, then this observation is consistent with the Faroes profile being closer to the centre of the mantle thermal anomaly created by the Iceland mantle plume than was the Hatton profile at the time the crust was generated. The full spreading rate of the crust between Hatton Bank and Greenland decreased from about 30 mm a^{-1} at 53 Ma (anomaly C24), to close to its present-day rate of 20 mm a^{-1} at the Reykjanes Ridge (Smallwood & White 2002).

As we discuss later, we ascribe these changes in crustal thickness to decreasing mantle temperatures following continental breakup. If for the moment we accept that the seafloor was generated by passive upwelling and decompression melting of mantle (Bown & White 1994), then the right-hand scale of Fig. 15 shows the mantle potential temperature that is required to generate the crustal thickness. Normal oceanic crust, averaged across segment lengths, is 6.4 ± 0.8 km

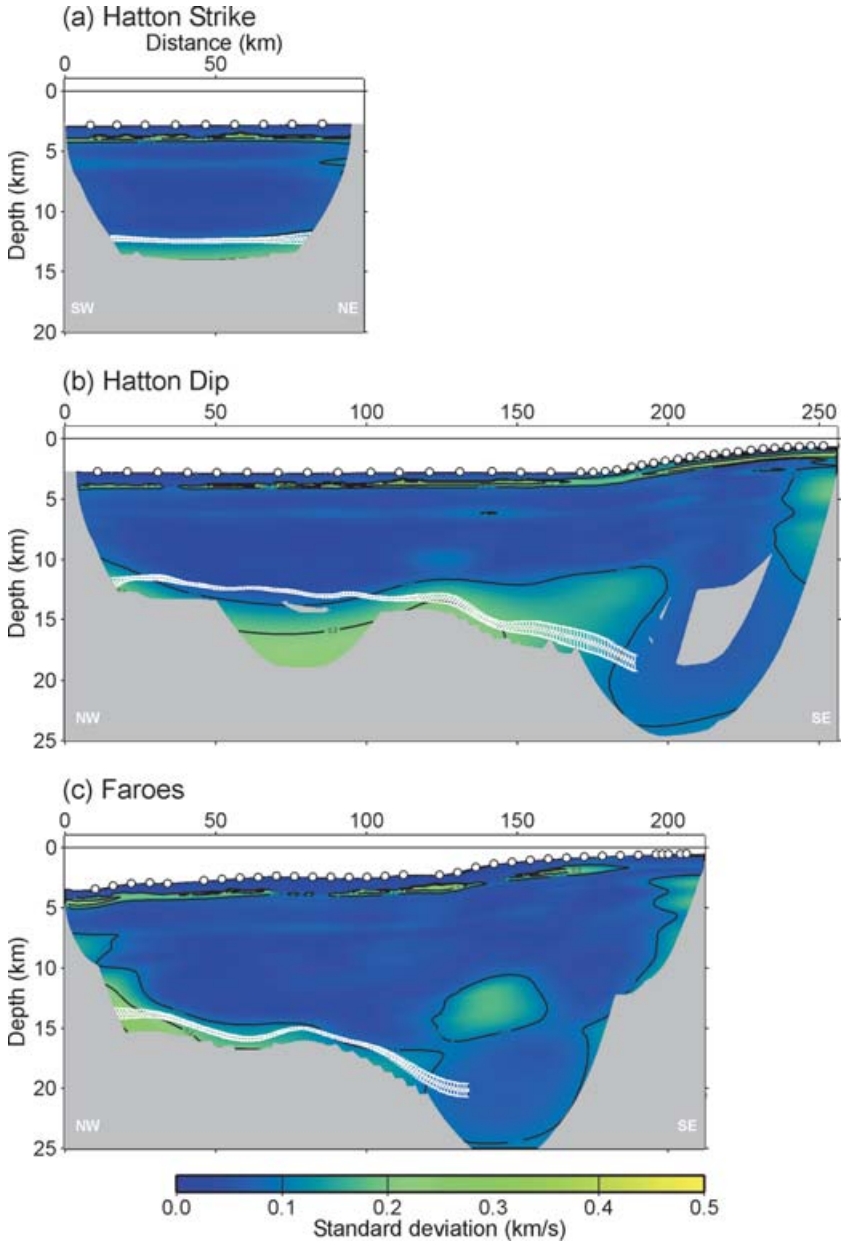

Figure 11. Standard deviation of each line following Monte Carlo analysis. White lines show position of the Moho with uncertainty estimates. Only those areas where there is ray coverage are shown.

thick (White *et al.* 1992), and formed from mantle with a potential temperature of ∼1300 °C. A decrease in mantle temperature of about 75 °C is required over the period of 9–12 Myr sampled by the Faroes and Hatton profiles (Fig. 15).

7.4 Mantle control on oceanic thickness and velocity

If mantle upwelling is a passive response to the plate separation at a seafloor spreading centre and is faster than a full spreading rate of about 15 mm a^{-1}, below which conductive cooling of the upwelling mantle reduces the amount of melting (Bown & White 1994), then for a given mantle composition, the amount of melt generated depends primarily on the mantle temperature. Provided the melt bleeds efficiently upward to freeze in the crust, which studies of the geochemistry and thickness of oceanic crust suggests is a good assumption (White *et al.* 2001), then the igneous crustal thickness can be used to infer the parent mantle temperature. Fig. 16(a) (solid lines) shows a compilation of theoretical curves of oceanic igneous thickness as a function of mantle potential temperature for passive upwelling and decompression melting of a dry pyrolitic mantle. These calculations assume that all the melt is accumulated in a 1-D section directly above the rift where it freezes to form the crust, and that the crust has zero porosity.

At first sight, the range in the different solid curves in Fig. 16(a) appears to be quite large. However, most of this range is caused by different legitimate choices for some of the parameters that constrain the melting models used to generate the theoretical curves, within the bounds of the uncertainty to which they are known. For example, White & McKenzie (1989) [W&McK 1989 on Fig. 16a] used a value for the entropy of melting of 250 J kg^{-1} $°C^{-1}$, whereas

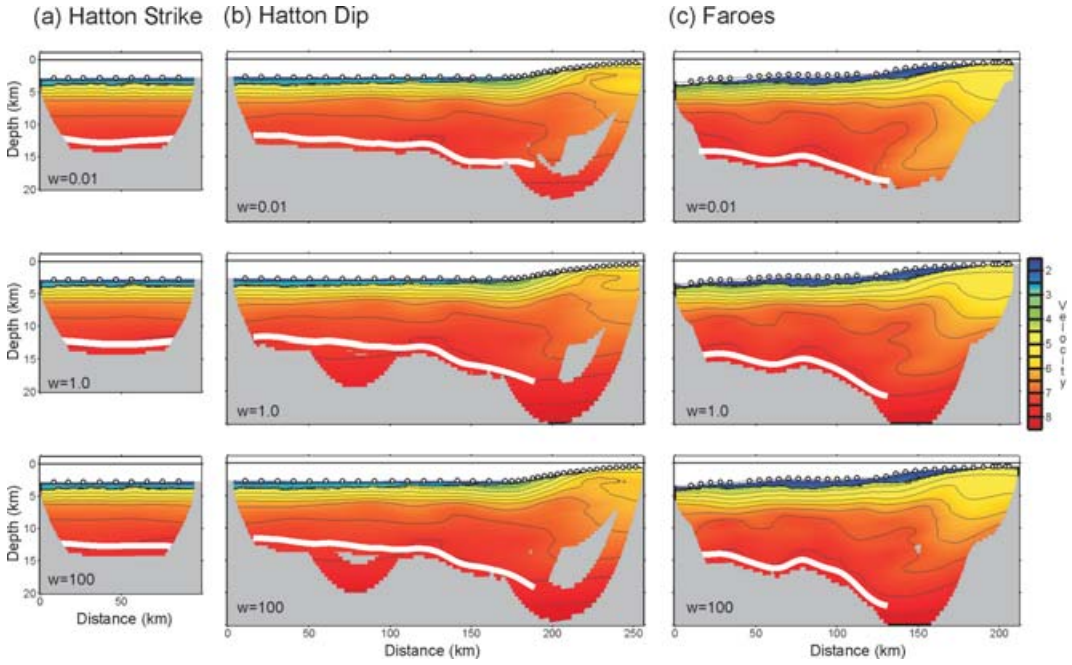

Figure 12. Velocity versus depth ambiguity tests for all profiles. Depth kernel weighting parameter, w, has been varied from $w = 0.01$ to 100 to investigate the trade-off between velocity and depth.

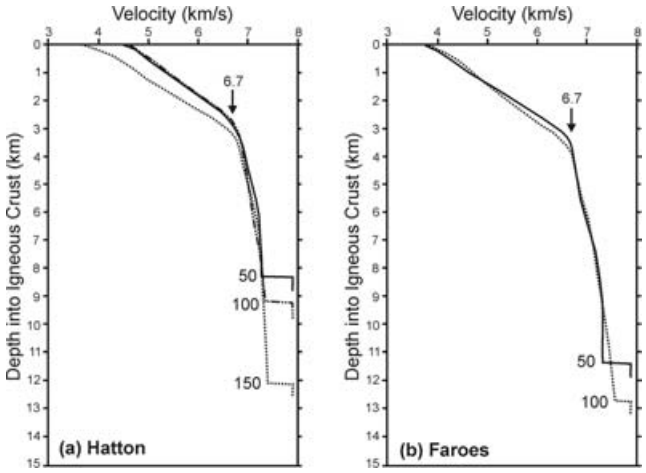

Figure 13. Representative velocity–depth profiles at 50 km intervals, with distances along profile labelled adjacent to Moho step, along (a) Hatton dip line and (b) Faroes line. The boundary between seismic Layer 2 and Layer 3 is at the inflexion point in the curves marked by arrow, at 6.7 km s^{-1}.

Bown & White (1994) [B&W 1994 on Fig. 16a] used a value of 400 J kg^{-1} °C^{-1}, and this makes a difference of 20–40 °C in the mantle temperature required to produce a given amount of melt, assuming all other factors are held fixed. Another significant uncertainty is the shape that is assumed for the melting region. However, the significant point to which we wish to draw attention is that the slopes of the different curves are closely similar for mantle potential temperatures higher than 1300 °C, the temperature at which normal oceanic crust is generated. This means that with any given melting model, we can deduce from the change in oceanic crustal thickness the increase in mantle temperature above that required to produce normal thickness oceanic crust (i.e. the mantle temperature anomaly), even though we cannot deduce the absolute mantle temperature with such precision.

The broken lines on Fig. 16(a) show calculations of the crustal thicknesses that result if the mantle has a more fertile component added. The representative fertile mantle source has 70 per cent depleted pyrolite mantle and 30 per cent MORB. As expected, the effect of this change in mantle composition is to cause more melt to be generated by decompression of mantle of a given temperature.

The results of a similar exercise to calculate the seismic velocity of the crust are illustrated in Fig. 16(b), where we show the theoretical *P*-wave seismic velocity of the crust formed from the primitive mantle melt when it freezes in the crust, as a function of the temperature of the parent mantle. The melt composition, and in particular its Mg, Fe and Si content, is dependent on the depth of melting, which in turn is controlled by the mantle temperature. White & McKenzie (1989) calculated the melt composition using the parametrization of McKenzie & Bickle (1988), and showed that the igneous crust would have higher velocities if the parent mantle were hotter. They calculated the seismic velocity of the rocks that crystallized from the melt by finding its CIPW norm and the Voight–Reuss–Hill average first for each mineral and then for the aggregate. Kelemen & Holbrook (1995) refined this by making empirical correlations of the composition of igneous rocks, while Korenaga *et al.* (2002) subsequently improved the theoretical calculations. Sallarès *et al.* (2005) introduced the possibility of a small amount of melting at depth in the presence of water in the mantle.

There is again considerable scatter in the curves in Fig. 16(b), although since the uncertainty in the calculations of the *P*-wave velocity is of the order of ±0.1 km s^{-1}, the curves made with similar assumptions are all within error of one another. However, as with the variation of crustal thickness with mantle temperature, the significant point is that the slopes of all the curves are closely similar above a normal mantle potential temperature of 1300 °C. So it is possible to determine from any of the curves the mantle temperature anomaly from the change in seismic velocity much more precisely than the absolute temperature. For a hypothetical fertile mantle comprising 70 per cent depleted pyrolite mantle and 30 per cent MORB (broken lines on Fig. 16b), the different mineralogy of the source

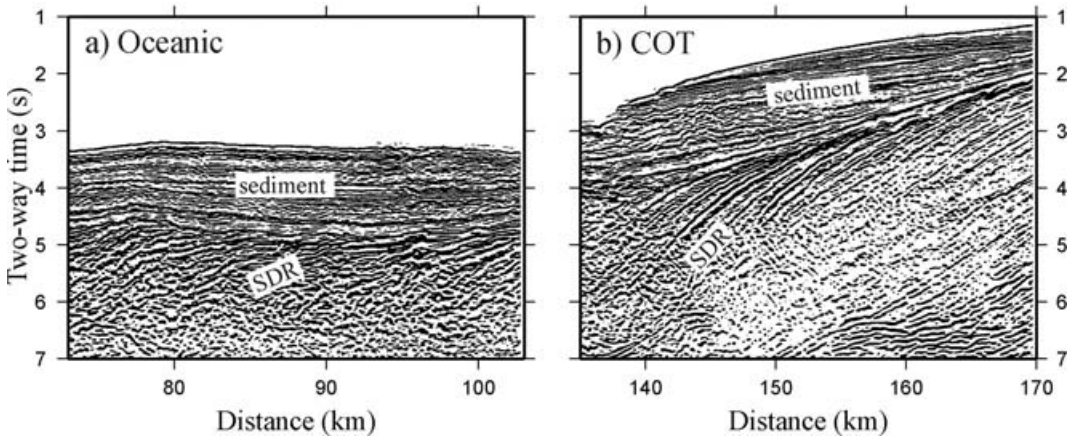

Figure 14. Seaward dipping reflectors imaged on the Faroes profile from migrated seismic reflection profile. (a) SDRs on thick oceanic crust are broken and irregular, formed from rifting in a submarine setting; (b) SDRs on continent–ocean transition are smooth and convex-upward, formed subaerially as basalts flowed landward from the elevated rift. Horizontal distances correspond to those on Fig. 2(b).

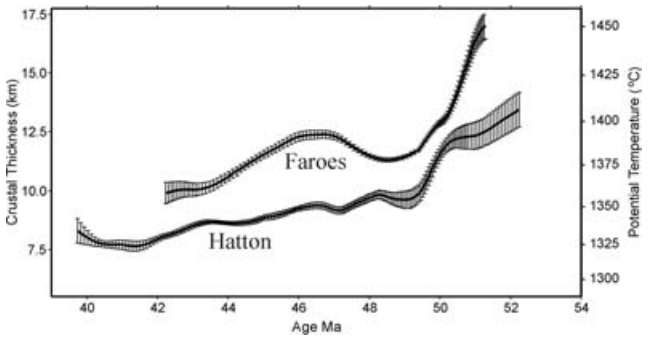

Figure 15. Total oceanic igneous crustal thickness variation with age for the Faroes and Hatton dip lines. Vertical bars show statistical uncertainties in thickness from multiple inversions with randomized starting models. Mantle potential temperature (right-hand side) is from the relationship of Bown & White (1994), which assumes melt generation is by passive decompression of the mantle beneath the spreading ridge. Both profiles show a rapid decrease in thickness for the first 5–6 Myr of seafloor spreading, with the thickness of the crust on the Faroes profile always greater than that of the same aged crust on the Hatton profile. The Faroes line also exhibits a pulse in thickness similar in amplitude and frequency to those that produce the V-shaped ridges south of Iceland at present, with much smaller fluctuations that are barely above the uncertainty present on the Hatton line.

means that the seismic velocity of material generated from mantle at a given temperature is reduced by between ∼0.2 km s^{-1} (Korenaga *et al.* 2002) and ∼0.35 km s^{-1} (Sallarès *et al.* 2005) compared to that formed by pyrolitic mantle.

The theoretical calculations shown in Fig. 16 all assume passive upwelling. However, it is possible that there was active upwelling beneath the seafloor spreading centre driven by convection in an underlying mantle plume. Active convection can explain, for example, the large volumes of melt generated above mantle plumes in intraplate settings such as Hawaii where there is no lithospheric rifting and the mantle decompression responsible for generating the melt is driven entirely by thermal convection (Watson & McKenzie 1991; White 1993). If there were active upwelling at the time of melt generation, then the crustal thickness alone could not be used to infer either the mantle temperature or the amount of active upwelling. This is because active convection would cause mantle to be cycled through the melting region, potentially generating large volumes of melt from small thermal anomalies in the mantle. So the curves in Fig. 16(a) would no longer give a direct link between mantle temperature and melt thickness.

In the case of the crustal seismic velocity, if there is active mantle convection through the melting region, then the melt composition would remain unchanged, however active the mantle convection, and so the seismic velocity of the rocks formed from that melt would remain little changed. This behaviour has the advantage for our purposes that the seismic velocity of the rocks may be used to constrain the mantle temperature, but the disadvantage that they cannot give any information on the amount of active upwelling.

An innovative method of inferring both the mantle temperature and the degree of active mantle upwelling responsible for the melt generation was developed by Kelemen & Holbrook (1995). They showed that the effect of mantle temperature and upwelling on the melt products could be separated if the total igneous crustal thickness, H, is plotted against the average bulk crustal velocity, V_p, in what we shall term an $H - V_p$ diagram. We show in Fig. 17 the theoretical curves from Fig. 16 for passive mantle upwelling plotted onto an $H - V_p$ diagram, with the curves plotted for a reference pressure of 230 MPa and an average temperature of 150 °C, which are representative of the lower-crust of the observed oceanic crustal data in our results. Note that both Korenaga *et al.* (2002) and Sallarès *et al.* (2005) plotted their curves using a reference pressure of 600 MPa and a reference temperature of 400 °C, so we applied a pressure correction of 0.2×10^{-3} km s^{-1} MPa^{-1} and a temperature correction of -0.4×10^{-3} km s^{-1} °C^{-1} (using the same pressure and temperature corrections as Korenaga *et al.* 2002). Also shown on Fig. 17 as a filled circle is the average thickness and average lower-crustal velocity of normal oceanic crust from White *et al.* (1992) with correction for along-segment variations in thickness as discussed by Bown & White (1994).

Perhaps the most difficult and uncertain issue in plotting observed data on an $H - V_p$ diagram is in choosing an appropriate measure of the bulk crustal velocity. The theoretical curves assume that the primary melt is frozen *in situ* in the crust without any differentiation either before or after it is emplaced in the crust. In reality, the melt ponds at sill-like magma chambers in the crust where it fractionates and indeed the melt may also undergo some subcrustal fractionation. As olivine is precipitated out, the residual melt becomes less dense, and what is eventually erupted to the surface with a MORB-type composition is this less dense residual melt, which freezes in the

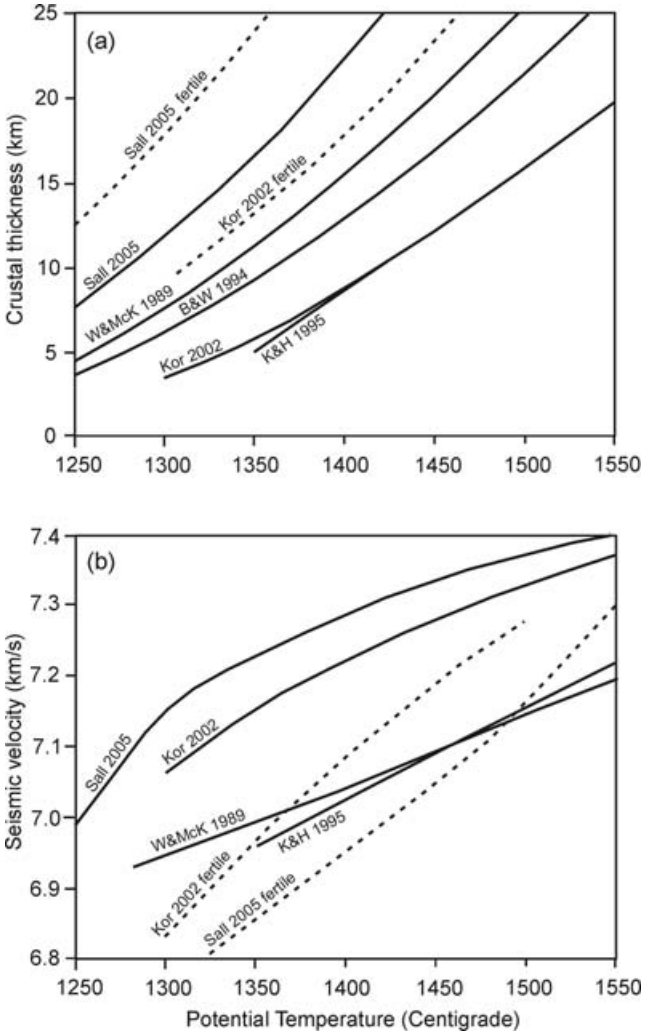

Figure 16. Theoretical calculations of (a) crustal thickness and (b) seismic velocity of primary melt frozen in the lower crust as a function of mantle potential temperature for dry pyrolitic mantle (solid lines) and fertile mantle comprising 70 per cent depleted pyrolite mantle and 30 per cent MORB (broken lines) as published by a range of authors. Curves are calculated for an average pressure of 230 MPa and an average temperature of 150 °C, which is representative of the average pressure and temperature conditions in the lower crust from the North Atlantic profiles discussed in this paper. Sources of curves: White & McKenzie (1989) [W&McK 1989]; Bown & White (1994) [B&W 1994]; Kelemen & Holbrook (1995) [K&H 1995]; Korenaga *et al.* (2002) [Kor 2002] and Sallarès *et al.* (2005) [Sall 2005].

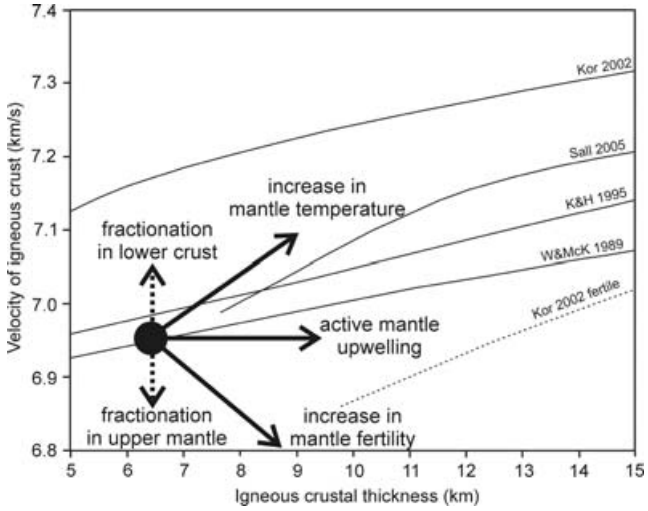

Figure 17. Theoretical igneous crustal thickness versus *P*-wave velocity of primary melt ($H - V_p$) curves for melt generated from normal pyrolitic mantle with passive upwelling curves are from White & McKenzie (1989) [W&McK 1989], Kelemen & Holbrook (1995) [K&H 1995], Korenaga *et al.* (2002) [Kor 2002], Sallarès *et al.* (2005) [Sall 2005] and from fertile mantle of Korenaga *et al.* (2002) [Kor 2002 fertile]. Curves are calculated for a reference pressure of 230 MPa and an average temperature of 150 °C, which are representative of the lower crust of the observed data in our results. Filled circle shows the thickness and average lower-crustal velocity of normal oceanic crust from White *et al.* (1992) with correction for along-segment variation in thickness as discussed by Bown & White (1994). Arrows show schematically the directions in which the lower crustal velocity and total igneous thickness would change due to the effects of: fractionation in the lower crust or upper mantle; an increase in the temperature of the parent mantle; active mantle upwelling under the oceanic rift; or an increase in the fertility of the parent mantle.

lower pressure and temperature conditions of the upper-crust to form a rock with lower seismic velocities than that of the rocks formed from the residual melt in the lower-crust. So it is likely that crustal fractionation causes the lower-crustal velocities to be slightly higher than the bulk velocity would otherwise have been (as shown by the upward-pointing dotted arrow on Fig. 17), while the upper-crust has reduced seismic velocities.

It is possible that some of the melt crystallizes in the mantle beneath the crust. Cannat (1996) suggests that perhaps 15–20 per cent of the melt may be trapped in the mantle beneath slow-spreading ridges, while Lizarralde *et al.* (2004) report observations of upper mantle velocities which they interpret as due to about 1.5 km (about 20 per cent) of the melt being trapped in the mantle where the spreading rate of oceanic crust in the western North Atlantic was below 20 mm a^{-1}. These relatively small amounts of melt are within the uncertainty of the agreement between geochemical and seismic measures of the amount of melt generated on slow-spreading ridges (White *et al.* 2001). Even where the crust is thick, as it is under present-day Iceland with its full spreading rate of 20 mm a^{-1}, pressure–temperature estimates suggest that some melt is intruded into the upper mantle (Maclennan *et al.* 2001). Korenaga *et al.* (2002) show that the effect of subcrustal fractionation would be to lower the seismic velocity of the residual melt which bleeds upward to freeze in the crust. The effect of subcrustal fractionation on the crustal bulk seismic velocity is greater when the bulk velocity is higher. For an average bulk crustal velocity of 7.15 km s^{-1}, which is typical of what we observe in our data (Fig. 18), melt retention in the mantle of 10–20 per cent would cause the bulk seismic velocity of the crust to be decreased by about 0.1 km s^{-1} (Korenaga *et al.* 2002). Since the effect on the lower-crustal velocity of subcrustal fractionation (downward-pointing dotted arrow on Fig. 17) operates in the opposite direction to the effect of crustal fractionation, and fortuitously with a similar magnitude, it suggests that it is a reasonable approximation to use the measured lower-crustal velocity as an estimate of the bulk velocity of the primary melt.

In addition to these fractionation effects on the seismic velocity, there is the more important effect of pore space, fractures and cracks in the upper crust which create the steep vertical velocity gradient of typically ∼1.0 s^{-1}, as seen in the upper 2–3 km of the velocity profiles in Fig. 13. Superimposed on the intrinsic velocities of the igneous crust caused by its composition and porosity is a downwards increase in velocity caused by the increasing pressure

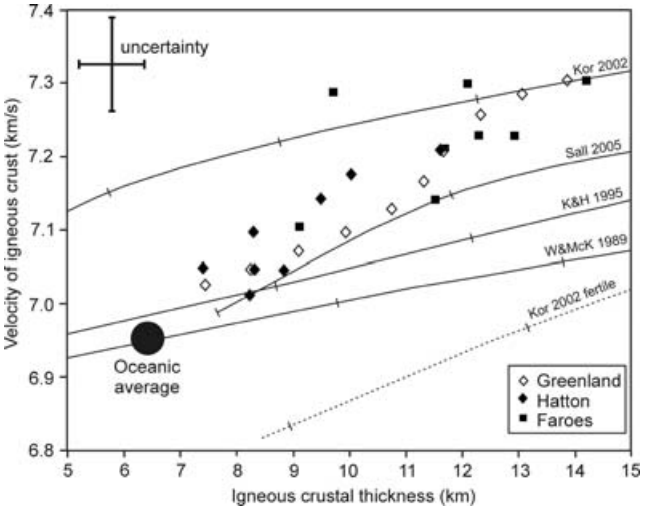

Figure 18. Average lower crustal velocity, V_p, and crustal thickness, H, for the Faroes profile (filled squares), the Hatton profile (filled diamonds), and the conjugate east Greenland SIGMA-III profile (open diamonds from Hopper *et al.* 2003) plotted with theoretical $H - V_p$ curves for primary melt generated from normal pyrolitic mantle with passive upwelling from White & McKenzie (1989) [W&McK 1989], Kelemen & Holbrook (1995) [K&H 1995], Korenaga *et al.* (2002) [Kor 2002], Sallarès *et al.* (2005) [Sall 2005], and from fertile mantle of Korenaga *et al.* (2002) [Kor 2002 fertile]. Tick marks on curves are at 50 °C increments in temperature (see Fig. 16 for values of potential temperature used to calculate curves). Thickness and average lower-crustal velocity of normal oceanic crust from White *et al.* (1992) with correction for along-segment variation in thickness as discussed by Bown & White (1994) is shown by filled circle. Average thicknesses and velocities are calculated with a 20 km window in distance and theoretical curves are calculated for the average pressure of 230 MPa and average temperature of 150 °C which are representative of the lower crust of the observed data. Uncertainty ranges typical of the data and of the theoretical curves are shown in the top left-hand corner of the diagram.

(P) and a downwards decrease in velocity caused by the increasing temperature (T) with depth. Rather than adjust our observed data to the average P, T conditions, we have chosen to calculate the H–V_p curves at the average P, T conditions appropriate for our data.

So how best to calculate the bulk crustal velocity from the observed data for comparison with the theoretical curves? Kelemen & Holbrook (1995) and Hopper *et al.* (2003) replaced all the upper-crustal material that had velocities of less than 6.8 km s^{-1}, with a uniform velocity of 6.8 km s^{-1} on the basis that the low velocities were caused primarily by the presence of pores, cracks and weathering, and that 6.8 km s^{-1} was a good representation of its intrinsic velocity. They then calculated the average velocity of the whole crust using these corrected velocities for the upper-crust. Korenaga *et al.* (2002) argued that the average velocity of the lower-crust alone was a better representation of the bulk crustal velocity, so they used only this section of the crust to calculate the average seismic velocity, though they calculated the crustal thickness H from the entire igneous section. Because the lower-crust contains the first fractionates from the primary melt, they argue that the velocity of the lower-crust is an upper bound on the bulk velocity, although as we noted earlier, for the typical lower-crustal velocities in our data, fractionation in the subcrustal region would tend to cause a reduction in velocity in the lower-crust which to first order is likely to be similar in magnitude to the increase caused by crustal fractionation. In this paper, we follow Korenaga *et al.*'s (2002) method of using the lower-crustal velocity as a proxy for the seismic velocity of the primary melt were it to freeze in the crust with its primary composition. The top of the lower-crust is defined by the inflexion point in the velocity–depth profiles at a velocity of 6.7 km s^{-1} (Fig. 13).

The bold arrows on Fig. 17 show the direction in which the lower-crustal velocities and whole crustal thicknesses would change under the specified changes in the mantle. For example, if the mantle temperature increased, but the upwelling remained passive, the seismic velocities on the $H - V_p$ diagram would move towards both higher thicknesses and higher velocities. If the mantle upwelled by active convection without any change in temperature, there would be an increase in thickness but no significant change in seismic velocity. This, therefore, provides a test which discriminates between the effect of increased mantle temperature and the presence of active upwelling if an increase of crustal thickness is observed along the profile. Finally, a change in mantle composition to a more fertile mantle would cause both a decrease in seismic velocity and an increase in crustal thickness.

7.5 Observational results from north Atlantic oceanic crust

The result of plotting our whole-crustal igneous thickness versus V_p measurements from the lower oceanic crust on the Faroes and Hatton lines is shown on a $H - V_p$ diagram in Fig. 18 by filled squares and diamonds, respectively. We also show measurements (open diamonds on Fig. 18) from the same aged oceanic crust on the east Greenland SIGMA-III profile which is approximately conjugate to the Hatton profile, using results from Hopper *et al.* (2003). Note that we have undone the replacement made by Hopper *et al.* (2003) of the upper-crust by material with a velocity of 6.8 km s^{-1}, and have instead used the lower-crustal velocity for direct comparison with our data. There is a strikingly close similarity of the $H - V_p$ data from the east Greenland side of the ocean with that from our new results on the NW European side as would be expected since the crust was formed at the same spreading centre. It is also clear that all the data lie on the same trend, a trend which points directly to the oceanic average shown by the filled circle on Fig. 18. All our observations show thicker crust with higher seismic velocities than normal oceanic crust.

The trend of the observed $H - V_p$ data from oceanic crust on both the Faroes and Hatton profiles shown on Fig. 18 is consistent with melting by passive decompression of normal dry, pyrolitic mantle (thin solid curves on Fig. 18) of variable temperature, with an end-member trending directly towards normal oceanic crust. Note that we have not included the uncertainty bars on the data (and they are of similar magnitude for the theoretical curves, too), which would have overwhelmed the plot, but instead show the representative uncertainty of the values in the top left-hand corner of Fig. 18. There is no evidence either of the presence of fertile source mantle (which would have moved the data points towards decreasing seismic velocities as the crustal thickness increased, see Fig. 17), or of active upwelling in the mantle (which would have produced a trend of increasing crustal thickness with little or no change in seismic velocity of the lower-crust, see Fig. 17).

The agreement is good between the trends of the data and the theoretical predictions for passive upwelling of mantle with a variable temperature (solid lines on Fig. 18), especially when the typical uncertainties are borne in mind. However, there is a faint indication that as the seismic thickness increases, the seismic velocity may be increasing slightly more than would be predicted theoretically from its increase in thickness. This is barely resolvable, given the

uncertainties in the velocity constraints, but nevertheless is in the opposite direction to the effects of either the presence of fertile mantle or of active upwelling (Fig. 17). However, it would be consistent with Korenaga *et al.*'s (2002) suggestion that the thicker oceanic crust may be slightly less prone to seismic velocity reduction by the presence of cracks in the lower crust than is the thinner oceanic crust. The change in average pressure in the lower-crust between the thickest and the thinnest crust on our profiles is only about 10 per cent, even though the crustal thickness varies by about 100 per cent, because the crust was generated, and has remained, in isostatic equilibrium. So we would not expect there to be large changes in seismic velocity resulting from pressure changes in the lower crust, nor for there to be large differences in the amount of cracking in the lower crust, and our observations of only a very small change in seismic velocity are in agreement with this expectation.

The overall trend of decreasing crustal thickness and decreasing V_p with age in our data is consistent with a trend of decreasing mantle temperature with age, heading towards normal oceanic crust, although always hotter than the mantle that produces normal oceanic crust. The inferred mantle temperature drop over the 10–12 Myr portions of the oceanic crust that we sample is ∼75 °C. The transition from subaerial to submarine SDRs on both sides of the Atlantic (Fig. 14 and Hopper *et al.* 2003) occurred at about the same time (51 Ma), as dynamic support from the mantle decreased, along with its decreasing temperature anomaly.

Similar decreases in crustal thickness, which are attributed to a drop in mantle temperature during the early seafloor spreading have been reported from oceanic crust of the same age adjacent to Edoras Bank, some 400 km along the continental margin to the south of the Hatton Bank survey (Barton & White 1997). About 800 km to the north of Iceland, off the Greenland margin, a similar decrease in oceanic thickness from 13.7 to 6.8 km occurs over the period 50.5–47.0 Ma on profile AW1-20030400 reported by Voss & Jokat (2007). Somewhat thinner oceanic crust, though with a complication caused by an 11.5 km thick igneous ridge, also shows a decrease in thickness over a similar period on profile AW1-20030500 which lies about 100 km to the south.

Also north of Iceland, but in the conjugate location on the European margin, similar decreases in oceanic crustal thickness are observed immediately after continental breakup off the Vøring margin (Mutter & Zehnder 1988; Mjelde *et al.* 2005). Nearer to our surveys, Breivik *et al.* (2006) report results from a profile across the Møre continental margin, some 400 km north of the Faroes profile, which also shows the igneous thickness decreasing by half over the interval from 52 to 42 Ma, although the reported oceanic crustal thickness is thinner than for the Vøring and Faroes margins which lie along strike on either side. We conclude that the decreases in oceanic thickness seen regionally in the first 10 Myr after continental breakup can be explained by a regional decrease in mantle temperature.

Away from the continental margin itself, subsidence of the Moray Firth prior to 49 Ma (Mackay *et al.* 2005), and of the NW European and Greenland basins prior to the mid-Eocene (∼45 Ma) (Mackay 2005) also suggests that continental breakup was followed by rapid subsidence. This is consistent with the reduction of regional dynamic support that can be explained by a regional decrease in the mantle temperature.

7.6 Pulsing of the Iceland mantle plume

In addition to the major decrease in mantle temperature recorded by the oceanic crust following continental breakup, there are superimposed fluctuations (Fig. 15), suggestive of the pulses which generate the V-shaped ridges seen on the Reykjanes Ridge. The Faroes profile younger than 49 Ma exhibits a pulse of increased thickness of ∼5 Myr duration with an amplitude of 2 km (equivalent to an increase in mantle temperature of ∼25 °C).

The thickened crust imaged on the Faroes profile using the seismic data also produces a linear positive anomaly in the gravity field off the Faroes (Fig. 19). Similar lineations are present within the gravity signature south of Iceland on both the western and eastern sides of the North Atlantic in crust older than magnetic chron 18 (some are marked by arrows on Fig. 19). The gravity lineations on the oldest oceanic crust south of Iceland are subdued due to the burial of the oceanic crust beneath thick sediments, but nonetheless are similar to the more prominent gravity lineations of the V-shaped ridges on the young crust of the Reykjanes Ridge where sediments are thin or absent. Seismic data shows that the recent V-shaped ridges on the Reykjanes Ridge are caused by crustal thickness variations of ∼2 km (Smallwood & White 1998). On the western side of the basin, off Greenland, it is clear that the gravity lineations (marked by arrows on Fig. 19) are oblique to the magnetic isochrons (chrons 18 and 21 are shown as thin black lines on Fig. 19), in the same way as are the recent V-shaped ridges near the present spreading centre. Weak gravity lineations of the same age occur on the eastern side of the oceanic basin off Hatton Bank (marked by arrows on Fig. 19), and there are some indications of concomitant crustal thickness increases on the Hatton seismic profile at ∼48 Ma (chron 21–22) and ∼39 Ma (chron 18) (Fig. 15).

This suggests that the pattern of mantle flow and its modulation by temperature fluctuations in the Iceland mantle plume have been maintained for the last 50 Ma since mature seafloor spreading commenced following continental breakup.

8 CONCLUSIONS

From our analysis of the seismic velocities and thicknesses of crust formed shortly after continental breakup in the North Atlantic we suggest that the earliest oceanic crust was generated from abnormally hot mantle, with a temperature anomaly of ∼100–150 °C above normal. Both the Faroes and Hatton regions show the oceanic crustal thickness gradually decreasing over time as the seafloor spreading continued, which we interpret as caused by a gradual decrease of ∼75 °C in the temperature of the mantle during the first 10–12 Myr of seafloor spreading. Similar decreases in crustal thickness, attributable to mantle temperature decreases, are reported from the oceanic crust formed off the Edoras, Møre and Vøring continental margins, which lie along the margin to the south and north of our profiles, and also from the oceanic crust formed adjacent to the east Greenland continental margin on the other side of the North Atlantic ocean. The change in morphology of the SDR sequences near the Faroes inferred as due to a change from subaerial to submarine extrusion is consistent with this decrease in mantle temperature as the dynamic support from the thermal anomaly in the mantle decreased. At all times the inferred mantle thermal anomaly near the Faroes was ∼30 °C higher than that of the Hatton region, consistent with its location closer to the centre of the Iceland mantle plume. We see no evidence of either active upwelling or of unusually fertile mantle during the period 52–40 Ma that we sample with our profiles since both mechanisms for generating melt would have produced igneous crust with lower seismic velocities than we observe at the igneous thicknesses found for our data.

Superimposed on the overall temperature decrease are thermal pulses of ∼25 °C which created linear ridges of thickened oceanic crust similar to those that form the V-shaped ridges of the

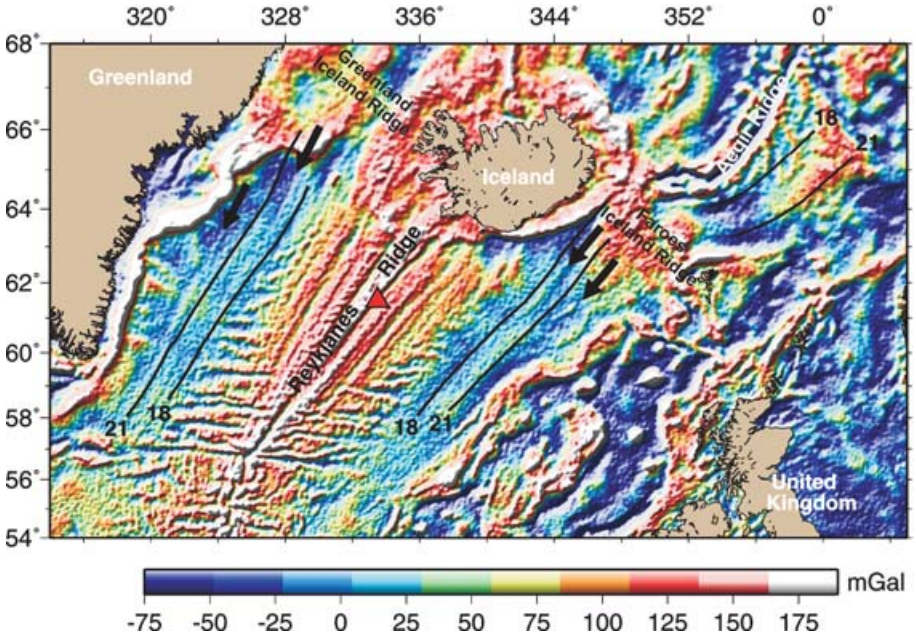

Figure 19. Free-air satellite gravity field (Sandwell & Smith 1997) illuminated from the northwest. Triangle shows location of seismic experiment by Smallwood & White (1998). Black lines show magnetic isochrons 18 (∼39 Ma) and 21 (∼48 Ma) from Müller *et al.* (1997). Arrows indicate some of the gravity lineations in the oldest oceanic crust thought to be generated by crustal thickness variations similar to those that cause the V-shaped ridges on the young oceanic crust at the present day.

Reykjanes Ridge during the Neogene. Lineations in the gravity field of the oldest oceanic crust formed south of Iceland suggest that the temperature of the Iceland mantle plume has been oscillating with a similar amplitude (∼25 °C) and periodicity (3–6 Myr), since at least 50 Ma. We note that it would be difficult to explain such frequent, regular and basin-wide fluctuations in crustal thickness that cause the gravity lineations using a model where the enhanced melting is caused solely by compositional rather than by thermal variations in the mantle, as suggested by Foulger (2002) and Foulger & Anderson (2005). Whether or not the mantle beneath Iceland is enriched by remnants of subducted plates, the widespread and well lineated crustal thickness variations can be readily explained by small variations in the temperature of the mantle as it flows outward from a central rising region in the vicinity of Iceland. It is likely that other mantle plumes exhibit similar fluctuating temperatures, although the small temperature variations cannot normally be detected because, unlike Iceland, the plumes do not directly underlie an oceanic spreading centre which provides a sensitive mantle thermometer where small mantle temperature fluctuations produce measurable crustal thickness variations.

ACKNOWLEDGMENTS

This work is part of the iSIMM project and would have been impossible without the enthusiastic support and commitment of our co-investigators. We thank particularly Alan W. Roberts for his assistance with the seismic data and Phil Christie for his advice and support. Jun Korenaga generously allowed us to use his tomographic inversion code tomo2D, as well as offering comments on this paper, Valentí Sallarès clarified details of his mantle melt modelling, and he and Harm Van Avendonk offered critical comments on the manuscript. Our interpretations, of course, remain our own. The iSIMM investigators are N. J. Kusznir, R. S. White, P. A. F. Christie, A. M. Roberts, A. Chappell, J. Eccles, R. Fletcher, D. Healy, N. Hurst, H. Lau, Z. Lunnon, C. J. Parkin, A. W. Roberts, L. K. Smith, R. Spitzer and V. Tymms. iSIMM was supported by Amerada Hess Ltd, Anadarko, BP, Conoco-Phillips, Eni-UK, Shell, Statoil, WesternGeco, the Natural Environment Research Council and the Department of Trade and Industry. C. J. Parkin also received funding from the Isle of Man Board of Education. Department of Earth Sciences, Cambridge contribution number ES8682.

REFERENCES

Anderton, R., Bridges, P.H., Leeder, M.R. & Sellwood, B.W., 1980. *A Dynamic Stratigraphy of the British Isles. A study in Crustal Evolution,* George, Allen and Unwin, 40 Museum street, London, UK.

Barker, P.F. & Hill, I.A., 1980. Asymmetric spreading in back-arc basins, *Nature,* **285,** 652–654.

Barton, A.J. & White, R.S., 1997. Crustal structure of the Edoras Bank continental margin and mantle thermal anomalies beneath the North Atlantic, *J. geophys. Res.,* **102,** 3109–3129.

Bickel, S.H., 1990. Velocity-depth ambiguity of reflection traveltimes, *Geophysics,* **55,** 266–276.

Bohnhoff, M. & Makris, J., 2004. Crustal structure of the southeastern Iceland-Faeroe Ridge (IFR) from wide angle aperture seismic data, *J. Geodyn.,* **37,** 233–252.

Bown, J.W. & White, R.S., 1994. Variation with spreading rate of oceanic crustal thickness and geochemistry, *Earth planet. Sci. Lett.,* **121,** 435–449.

Braun, M.G., Hirth, G. & Parmentier, E.M., 2000. The effects of deep damp melting on mantle flow and melt generation beneath mid-ocean ridges, *Earth planet. Sci. Lett.,* **176,** 339–356.

Breivik, A.B., Mjelde, R., Faleide, J.I. & Murai, Y., 2006. Rates of continental breakup magmatism and seafloor spreading in the Norway Basin–Iceland Plume interaction, *J. geophys. Res.,* **111,** B0712, doi: 10.1029/2005JB004004.

Cande, S.C. & Kent, D.V., 1992. A new geomagnetic polarity time scale for the Late Cretaceous and Cenozoic, *J. geophys. Res.,* **97**(B10), 13 917–13 951.

Cannat, M., 1996. How thick is the magmatic crust at slow spreading oceanic ridges? *J. geophys. Res.,* **101**(B2), 2847–2857.

Chambers, L.M., Pringle, M.S. & Parrish, R.R., 2005. Rapid formation of the Small Isles Tertiary centre constrained by precise $^{40}Ar/^{39}Ar$ and U-Pb ages, *Lithos,* **79,** 367–384.

Cole, P.B., Minshull, T.A. & Whitmarsh, R.B., 2002. Azimuthal seismic anisotropy in a zone of exhumed continental mantle, West Iberia margin, *Geophys. J. Int.,* **151,** doi:10.1046/j.1365-246X.2002.01781.x.

Darbyshire, F.A., White, R.S. & Priestley, K.F., 2000. Structure of the crust and uppermost mantle of Iceland from a combined seismic and gravity study, *Earth planet. Sci. Lett.,* **181,** 409–428.

Dóre, A.G., Fichler, C. & Olesen, O., 1997. Patterns of basement structure and reactivation along the NE Atlantic margin, *J. Geol. Soc. Lond.,* **154,** 85–92.

England, R.W. & Hobbs, R.W., 1997. The structure of the Rockall Trough imaged by deep seismic reflection profiling, *J. Geol. Soc. Lond.,* **154,** 497–502.

Fitton, J.G., Larsen, L.M., Saunders, A.D., Hardarson, B.S. & Kempton, P.D., 2000. Paleocene continental to oceanic magmatism on the SE Greenland Margin at 63°N: a review of the results of the Ocean Drilling Program Legs 152 and 163, *J. Petrol,* **41,** 951–966.

Foulger, G.R., 2002. Plumes, or plate tectonic processes, *Astron. Geophys.,* **43,** 6.19–6.23.

Foulger, G.R. & Anderson, D.L., 2005. A cool model for the Icelandic hotspot, *J. Volc. Geotherm. Res.,* **141,** 1–22.

Fowler, S.R., White, R.S., Spence, G.D. & Westbrook, G.K., 1989. The Hatton Bank continental margin II. Deep structure from two-ship expanding spread seismic profiles, *Geophys. J. Int.,* **96,** 295–309.

Gill, R.C.O., Holm, P.M. & Nielsen, T.F.D., 1995. Was a short-lived Baffin Bay plume active prior to initiation of the present Icelandic plume? Clues from the high-Mg picrites of West Greenland, *Lithos,* **34,** 27–39.

Gregg, T.K. P. & Fornari, D.J., 1998. Long submarine lava flows: Observations and results from numerical modeling, *J. geophys. Res.,* **103,** 27 517–27 531.

Gubbins, D., 2004. *Time Series Analysis and Inverse Theory for Geophysicists,* Cambridge University Press, Cambridge, UK.

Holbrook, W.S. *et al.*, 2001. Mantle thermal structure and active upwelling during continental breakup in the North Atlantic, *Earth planet. Sci. Lett.,* **190,** 251–266.

Hopper, J.R., Dahl-Jensen, T., Holbrook, W.S., Larsen, H.C., Lizarralde, D., Korenaga, J., Kent, G.M. & Kelemen, P.B., 2003. Structure of the SE Greenland margin from seismic reflection and refraction data: implications for nascent spreading center subsidence and asymmetric crustal accretion during North Atlantic opening, *J. geophys. Res.,* **B5,** doi:10.1029/2002JB001996.

Houseman, G.A., 1990. The thermal structure of mantle plumes: axisymmetric or triple junction? *Geophys. J. Int.,* **102,** 15–24.

Ito, G., 2001. Origin of V-Shaped Reykjanes Ridges from a Pulsing and Dehydrating Mantle Plume, *Nature,* **411,** 681–684.

Ito, G., Shen, Y., Hirth, G. & Wolfe, C.J., 1999. Mantle flow, melting, and dehydration of the Iceland mantle plume, *Earth planet. Sci. Lett.,* **165,** 81–96.

Jolley, D.W. & Bell, B.R., 2002. The evolution of the North Atlantic Igneous Province and the opening of the NE Atlantic rift, in *The North Atlantic Igneous Province: Sratigraphy, Tectonic and Magmatic Processes,* Vol. 197, pp. 1–13, eds Bell, B. & Jolley, D., Spec. Publ. J. Geol. Soc., London.

Jones, S.M. & White, N., 2003. Shape and size of the starting Iceland plume swell. *Earth planet. Sci. Lett.,* **216,** 271–282.

Jones, S.M., White, N. & Maclennan, J., 2002. V-shaped ridges around Iceland: implications for spatial and temporal patterns of mantle convection, *Geochem. Geophys. Geosyst.,* **3**(10), doi:10.1029/2002GC000361.

Kelemen, P.B. & Holbrook, W.S., 1995. Origin of thick, high-velocity igneous crust along the U.S. East Coast Margin, *J. geophys. Res.,* **100**(B7), 10 077–10 094.

Kent, R.W., 1995. Magnesium basalts from the Hebrides, Scotland: chemical composition and relationship to the Iceland plume, *J. Geol. Soc. Lond.,* **152,** 979–983.

Kharin, G.N. *et al.*, 1976. *Initial Reports of the Deep Sea Drilling Project,* Vol. 38, pp. 755–759, U.S. Govt. Print. Off., Washington, DC.

Klein, E.M. & Langmuir, C.H., 1987. Global correlations of ocean ridge basalt chemistry with axial depth and crustal thickness, *J. geophys. Res.,* **92,** 8089–8115.

Korenaga, J., 2004. Mantle mixing and continental breakup magmatism, *Earth planet. Sci. Lett.,* **218,** 463–473.

Korenaga, J., Holbrook, W.S., Kent, G.M., Kelemen, P.B., Detrick, R.S., Larsen, H.C., Hopper, J.R. & Dahl-Jensen, T., 2000. Crustal structure of the southeast Greenland margin from joint refraction and reflection seismic tomography, *J. geophys. Res.,* **105**(B9), 21 591–21 614.

Korenaga, J., Kelemen, P.B. & Holbrook, W.S., 2002. Methods for resolving the origin of large igneous provinces from crustal seismology, *J. geophys. Res.,* **107**(B9), doi:10.1029/2001JB001030.

Larsen, H.C. & Jakobsdóttir, S., 1988. Distribution, crustal properties and significance of seawards-dipping sub-basement reflectors off E Greenland, in *Early Tertiary Volcanism and the Opening of the NE Atlantic,* vol. 39, pp. 95–114, eds Morton, A.C. & Parson, L.M., Spec. Pub. Geol. Soc., London.

Larsen, H.C. & Saunders, A.D., 1998. Tectonism and volcanism at the southeast Greenland rifted margin: a record of plume impact and later continental rupture, in *Proc. ODP, Sci. Results,* Vol., 152, pp. 503–533, eds Saunders, A.D., Larsen, H.C. & Wise, S.W., Jr., Ocean Drilling Program, College Station, TX.

Lizarralde, D., Gaherty, J.B., Collins, J.A., Hirth, G. & Kim, S.D., 2004. Spreading-rate dependence of melt extraction at mid-ocean ridges from mantle seismic refraction data, *Nature,* **432,** 744–747.

Lunnon, Z.C., Christie, P.A.F. & White, R.S., 2003. An evaluation of peak and bubble tuning in sub-basalt seismology: modelling and results from OBS data, *First Break,* **21**(12), 51–56.

Mackay, L.M., 2005. Cenozoic Vertical Motions in the North Atlantic Region, *PhD dissertation*, Department of Earth Sciences, University of Cambridge.

Mackay, L.M., Turner, J., Jones, S.M. & White, N.J., 2005. Cenozoic vertical motions in the Moray Firth Basin associated with initiation of the Iceland Plume, *Tectonics,* **24**(TC5004), doi:10.1029/2004TC001683.

Maclennan, J., McKenzie, D., Gronvold, K. & Slater, L., 2001. Crustal accretion under northern Iceland, *Earth planet. Sci. Lett.,* **191,** 295–310.

McBride, J.H., Henstock, T.J., White, R.S. & Hobbs, R.W., 1994. Seismic reflection profiling in deep water: avoiding spurious reflectivity at lower crustal and upper-mantle traveltimes, *Tectonophysics,* **232,** 425–435.

McKenzie, D. & Bickle, M.J., 1988. The volume and composition of melt generated by extension of the lithosphere, *J. Petrol.,* **29,** 625–679.

Mjelde, R., Kodaira, S., Shimamura, H., Kanazawa, T., Shiobara, H., Berg, E.W. & Ruse, O., 1997. Crustal structure of the central part of the Vøring basin, mid-Norway margin, from ocean-bottom seismographs, *Tectonophysics,* **277,** 235–257.

Mjelde, R., Digranes, P., Shimamura, H., Kodaira, S., Brekke, H., Egebjerg, N., Sorenses, N. & Thorbjornses, S., 1998. Crustal structure of the northern part of the Vøring basin, mid-Norway margin, from wide-angle seismic and gravity data, *Tectonophysics,* **293,** 175–205.

Mjelde R., Raum, T., Myhren, B., Shimamura, H., Murai, Y., Takanami, T., Karpuz, R. & Naess U., 2005. Continent-ocean transition on the Vøring Plateau, NE Atlantic, derived from densely sampled ocean bottom seismometer data, *J. geophys. Res.,* **110,** B05101, doi:10.1029/2004JB003026.

Morgan, J.V., Barton, P.J. & White, R.S., 1989. The Hatton Bank continental margin – III. Structure from wide-angle OBS and multichannel seismic refraction profiles, *Geophys. J. Int.,* **98,** 367–384.

Mosegaard, K. & Sambridge, M., 2002. Monte Carlo analysis of inverse problems, *Inverse Problems,* **18**(R29-R54), doi:10.1088/0266-5611/18/3/201.

Müller, R.D., Roest, W.R., Royer, J.Y., Gahagan, L.M. & Sclater, J.G., 1997. Digital isochrons of the world's ocean floor, *J. geophys. Res.,* **102**(B2), 3211–3214.

Mutter, J.C. & Zehnder, C.M., 1988. Deep crustal and magmatic processes: The inception of seafloor spreading in the Norwegian–Greenland sea, in *Early Tertiary Volcanism and the Opening of the NE Atlantic,* Vol. 39, pp. 35–48, eds Morton, A.C. & Parson, L.M., Spec. Pub. Geol. Soc., London.

Mutter, J.C., Talwani, M. & Stoffa, P.L., 1982. Origin of seaward-dipping reflectors in oceanic crust off the Norwegian margin by subaerial sea-floor spreading, *Geology,* **10,** 353–337.

Nadin, P.A. & Kusznir, N.J., 1995. Palaeocene uplift and Eocene subsidence in the northern North Sea Basin from 2D forward and reverse stratigraphic modelling, *J. Geol. Soc. Lond.,* **152,** 833–848.

Nakamura, Y., Donoho, P.L., Roper, P.H. & McPherson, P.M., 1987. Large-offset seismic surveying using ocean bottom seismograms and airguns: instrumentation and field technique, *Geophysics,* **52,** 1601–1611.

Nielsen, T.K. & Hopper, J.R., 2004. From rift to drift: mantle melting during continental breakup, *Geochem. Geophys. Geosyst.,* **5**(7), doi:10.1029/2003GC000662.

Nielsen, T.K., Larsen, H.C. & Hopper, J.R., 2002. Contrasting rifted margin styles south of Greenland: implications for mantle plume dynamics, *Earth planet. Sci. Lett.,* **200,** 270–285, doi:10.1016/S0012-821X(02)0,616-7.

O'Connor, J.M., Stoffers, P., Wijbrans, J.R., Shannon, P.M. & Morrissey, T., 2000. Evidence from episodic seamount volcanism for pulsing of the Iceland plume in the past 70 Myr, *Nature,* **408,** 954–958.

Parkin, C.J., Lunnon, Z.C., White, R.S. & Christie, P.A.F., 2007. Imaging the pulsing Iceland mantle plume through the Eocene, *Geology,* **35,** 93–96.

Planke, S., Symonds, P.A., Alvestad, E. & Skogseid, J., 2000. Seismic volcanostratigraphy of large-volume basaltic extrusive complexes on rifted margins, *J. geophys. Res.,* **105,** 19 335–19 351.

Poore, H.R., Samworth, R.J., White, N.J., Jones, S.M. & McCave, I.N., 2006. Neogene overflow of northern component water at the Greenland-Scotland ridge, *G3 Geochemistry Geophysics Geosystems,* **7,** Q06010, doi:10.1029/2005GC001085.

Raitt, R.W., Shor, G.G., Francis, T.J.G. & Morris, G.B., 1969. Anisotropy of the Pacific upper mantle, *J. geophys. Res.,* **74**(12), 3095–3109.

Roberts, A.W., 2006. Crustal structure of the Faroes North Atlantic margin from wide-angle seismic data. *PhD dissertation,* University of Cambridge, 230 pp.

Roberts, A.W., White, R.S., Lunnon, Z.C., Christie, P.A. F., Spitzer, R. & iSIMM Team, 2005. Imaging magmatic rocks on the Faroes margin, in *Petroleum Geology: North-West Europe and Global Perspectives, Proceedings of the 6th Petroleum Geology Conference,* pp. 755–766, eds Dore, A.G. & Vining, B.A., Geological Society of London.

Sallarès, V., Charvis, P., Flueh, E.R., Bialas, J. & the SALIERI Scientific Party, 2005. Seismic structure of the Carnegie ridge and the nature of the Galápagos hotspot, *Geophys. J. Int.,* **161,** 763–788, doi:10.1111/j.1365-246X.2005.02592.x.

Sandwell, D.T. & Smith, W.H.F., 1997. Marine gravity from Geosat and ERS 1 satellite altimetry, *J. geophys. Res.,* **102,** 10 039–10 054.

Saunders, A.D., Fitton, J.G., Kerr, A.C., Norry, M.J. & Kent, R.W., 1997. The North Atlantic Igneous Province, in *Large Igneous Provinces: Continental, Oceanic and Planetary Flood Volcanism,* Vol. 100, pp. 45–93, eds Mahoney, J. & Coffin, M., Geophys. Mon., Amer. Geophys. Union, Washington DC, USA.

Scott, R.A., Ramsey, L.A., Jones, S.M., Sinclair, S. & Pickles, C.S., 2005. Development of the Jan Mayan microcontinent by linked propogation and retreat of spreading ridges, in *Onshore-Offshore Relationships on the North Atlantic Margin,* Vol. 12, pp. 69–82, eds Wandås, B.T.G., Nystuen, J.P., Eide, E. & Gradstein, F., Norw. Petrol. Soc. Spec. Publ., Elsevier, Amsterdam.

Smallwood, J.R. & White, R.S., 1998. Crustal accretion at the Reykjanes Ridge 61°–62°N, *J. geophys. Res.,* **103,** 5185–5201.

Smallwood, J.R. & White, R.S., 2002. Ridge-plume interactions in the North Atlantic and its influence on continental breakup and seafloor spreading, in *The North Atlantic Igneous Province: Stratigraphy, Tectonic and Magmatic Processes,* Vol. 197, pp. 15–37, eds Bell, B. & Jolley, D., Spec. Pub. Geol. Soc., London.

Smallwood, J.R., Staples, R.K., Richardson, R. & White, R.S., 1999. Crust generated above the Iceland mantle plume: from continental rift to oceanic spreading center, *J. geophys. Res.,* **104**(B10), 22 885–22 902.

Spakman, W. & Nolet, G., 1988. Imaging algorithms, accuracy, and resolution in delay time tomography, in *Mathematical Geophysics,* pp. 155–187, eds Vlaar, N.J., Nolet, G., Wortel, M.J.R. & Cloetingh, S.A.P.L., D. Reidel Publishing Company, Dordrecht, The Netherlands.

Spence, G.D., White, R.S., Westbrook, G.K. & Fowler, S.R., 1989. The Hatton Bank continental margin I. Shallow structure from two-ship expanding spread seismic profiles, *Geophys. J. Int,* **96,** 273–294.

Spitzer, R., White, R.S. & The iSIMM team, 2005. Advances in seismic imaging through basalts: a case study from the Faroe-Shetland Basin, *Petrol. Geosci.,* **11,** 147–156.

Srivastava, S.P., 1978. Evolution of the Labrador Sea and its bearing on the early evolution of the North Atlantic, *Geophys. J. R. astr. Soc,* **52,** 313–355.

Tarantola, A., 2005. *Inverse Problem Theory and Methods for Model Parameter Estimation,* Society for Industrial and Applied Mathematics, 3600 University City Science Center, Philadelphia, PA, USA.

Verhoef, J., Roest, W.R., Macnab, R., Arkani-Hamed, J. & Members of the Project Team, 1996. Magnetic anomalies of the Arctic and North Atlantic oceans and adjacent land areas, Open File 3125a, Geological Survey of Canada.

Vogt, P.R., 1971. Asthenosphere motion recorded by the ocean floor south of Iceland, *Earth planet. Sci. Lett.,* **13,** 153–160.

Voss, M. & Jokat, W., 2007. Continent-ocean transition and voluminous magmatic underplating derived from P-wave velocity modelling of the East Grenland continental margin, *Geophys. J. Int.,* **170,** 580–604.

Watson, S.P. & McKenzie, D.P., 1991. Melt generation by plumes: a study of Hawaiian volcanism, *J. Petrol.,* **32,** 501–537.

White, R.S., 1993. Melt production rates in mantle plumes. *Phil. Trans. Roy. Soc., Lond., Ser. A,* **342,** 137–153.

White, R.S., 1997. Rift-plume interaction in the North Atlantic, *Philos. Trans. Roy. Soc. Lond.,* **355**(A), 319–339.

White, N. & Lovell, B., 1997. Measuring the pulse of a plume within the sedimentary record, *Nature,* **387,** 888–891.

White, R. & McKenzie, D., 1989. Magmatism at rift zones: the generation of volcanic continental margins and flood basalts, *J. geophys. Res.,* **94,** 7685–7729.

White, R.S., Spence, G.D., Fowler, S.R., McKenzie, D., Westbrook, G.K. & Bowen, A.N., 1987. Magmatism at rifted continental margins, *Nature,* **330,** 439–444.

White, R.S., McKenzie, D. & O'Nions, K., 1992. Oceanic crustal thickness from seismic measurements and rare earth element inversions, *J. geophys. Res.,* **97**(B13), 19 683–19 715.

White, R.S., Bown, J.W. & Smallwood, J.R., 1995. The temperature of the Iceland plume and the origin of outward propagating V-shaped ridges, *J. Geol. Soc. Lond.,* **152,** 1039–1045.

White, R.S., Minshull, T.A., Bickle, M.J. & Robinson, C.J., 2001. Melt generation at very slow-spreading oceanic ridges: constraints from geochemical and geophysical data. *J. Petrol.,* **42,** 1171–1196.

White, R.S. *et al.*, 2002. iSIMM pushes frontiers of marine seismic acquisition, *First Break,* **20**(12), 782–786.

Wright, J.D. & Miller, K.G., 1996. Control of North Atlantic deep water circulation by the Greenland-Scotland Ridge, *Palaeoceanography,* **11,** 157–170.

Zehnder, C.M., Mutter, J.C. & Buhl, P., 1990. Deep seismic and geochemical constraints on the nature of rift-induced magmatism during breakup of the North Atlantic, *Tectonophysics,* **173,** 545–565.

Zelt, C.A., 1999. Modelling strategies and model assessment for wide-angle seismic traveltime data, *Geophys. J. Int.,* **139,** 183–204.

Zelt, C.A. & Smith, R.B., 1992. Seismic traveltime inversion for 2-D crustal velocity structure, *Geophys. J. Int.,* **108,** 16–34.

Zhang, J. & Toksöz, M.N., 1998. Nonlinear refraction traveltime tomography, *Geophysics,* **63**(5), 1726–1737.

Ziegler, P.A., 1989. Evolution of the North Atlantic—an overview, in *Extensional Tectonics and Stratigraphy of the North Atlantic Margin,* Vol. 46, pp. 111–129, eds Tankard, A. & Balkwill, H., American Association of Petroleum Geologists, 125 West 15th Street, Tulsa, OK 74119, USA.

Ziolkowski, A., Parkes, G., Hatton, L. & Haugland, T., 1982. The signature of an air-gun array—computation from near-field measurements including interactions, *Geophysics,* **51,** 169–182.